Showcasing research from Professor Simon Lux's group at the University of Münster and Fraunhofer FFB in Münster, Germany.

Benchmarking state-of-the-art sodium-ion battery cells – modeling energy density and carbon footprint at the gigafactory-scale

Sodium-ion batteries (SIBs) are emerging as an alternative to lithium-ion batteries (LIBs), using abundant, low-cost materials. This study models commercially relevant SIB cell chemistries at industrial scale. While current SIBs have 17–49% lower energy density than LiFePO$_4$/graphite LIBs, this gap could be closed through material improvements of hard carbon. In terms of carbon footprint, SIBs are already comparable to LIBs and could further reduce emissions as energy density increases. The analysis, based on large-format cells and gigafactory-scale production data, addresses a key research gap beyond lab-scale data.

Image reproduced by permission of Tyll Farnschlaeder, Fraunhofer FFB from *Energy Environ. Sci.*, 2025, **18**, 8104. Partially generated with AI tools.

As featured in:

See Simon Lux *et al.*,
Energy Environ. Sci., 2025, **18**, 8104.

ROYAL SOCIETY
OF **CHEMISTRY**

rsc.li/ees

Registered charity number: 207890

ANALYSIS

Check for updates

Benchmarking state-of-the-art sodium-ion battery cells – modeling energy density and carbon footprint at the gigafactory-scale†

Philipp Voß, [ab] Benedikt Gruber, [bc] Miriam Mitterfellner, [b] Jan-Darius Plöpst, [b] Florian Degen, [b] Richard Schmuch [b] and Simon Lux [*ab]

Sodium-ion batteries (SIBs) are on the verge of mass adoption, with several players striving for gigafactory-scale production. Uncertainty remains regarding their competitiveness with lithium-ion batteries (LIBs). This study addresses this concern by quantifying the energy density and carbon footprint (CF) of commercially pursued SIB cell chemistries through comprehensive modeling. Multiple material and production scenarios are analyzed, with LiFePO$_4$ (LFP)-based LIB cells serving as an industry benchmark. Based on a screening of commercially relevant SIB active materials, the volumetric and gravimetric energy content is modeled for large-format pouch and prismatic cells, as well as varying cathode coating thickness. Additionally, a GWh year^{-1} cell production is simulated using primary machine data and current production equipment. The outputs from cell and production modeling feed into a life cycle assessment to determine the CF by calculating the cradle-to-gate global warming potential, relative to the cell energy [kg CO$_2$-eq. kWh^{-1}]. Additionally, new life cycle inventory data are presented for the industrial-scale synthesis of hard carbon (HC) and SIB-cathode active materials (CAMs). Current SIB cells show notably lower energy content compared to the LFP benchmark, particularly in terms of volumetric energy density (Δ = 17–49%). However, this gap could be narrowed and even closed for specific SIB cell chemistries through optimization of HC, representing a near-future scenario. While HC is the bottleneck towards higher energy density, the opposite is true for the CF. Among the seven evaluated SIB cell chemistries, four demonstrate CFs that are highly competitive with the LFP benchmark (Δ = 1–8%), despite exhibiting lower energy densities. This is primarily due to the substantially lower CF of HC (3.2 kg CO$_2$-eq. kg^{-1}) compared to synthetic graphite (25.1 kg CO$_2$-eq. kg^{-1}). In contrast, LFP-CAM (7.6 kg CO$_2$-eq. kg^{-1}) causes fewer emissions than six of the seven analyzed SIB-CAMs (5.8 kg CO$_2$-eq. kg^{-1} to 22.0 kg CO$_2$-eq. kg^{-1}). The key factors for further CF reduction in SIBs are the application of low-impact CAMs and increasing energy density. In contrast, transitioning to aqueous cathode processing was found to only have a small impact on the cell-level CF, considering state-of-the-art *N*-methyl-2-pyrrolidone recovery techniques.

Broader context

Batteries are essential to the transition towards a climate-neutral energy system. While lithium-ion batteries (LIBs) dominate the market due to their high energy density and long cycle life, their reliance on geographically constrained and costly raw materials like lithium and cobalt has raised concerns about long-term sustainability, resource availability, and environmental impact. Sodium-ion batteries (SIBs) are gaining attention as a sustainable alternative to LIBs. SIBs benefit from abundant, low-cost, and globally distributed raw materials, making them a promising energy storage solution. Consequently, several cell manufacturers are actively pursuing gigafactory-scale production of SIBs and the technology is on the verge of mass adoption. Recent studies have analyzed the energy density and environmental impact of SIBs, however, the depth of the literature remains limited compared to studies covering LIBs and does not address cells at a commercial scale. While existing studies generally rely on lab-scale data, this work focuses on industrial active material synthesis, large-format cells and gigawatt-hour scale production. Cell chemistries from leading SIB manufacturers are benchmarked against graphite/LiFePO$_4$ LIB cells and assessed for specific energy, energy density, and cradle-to-gate carbon footprint.

[a] *Institute of Business Administration at the Department of Chemistry and Pharmacy, University of Münster, Leonardo Campus 1, 48149 Münster, Germany.*
 E-mail: simon.lux@uni-muenster.de

[b] *Fraunhofer Research Institution for Battery Cell Production FFB, 48165 Münster, Germany*

[c] *Chair for Production Engineering of E-Mobility Components, RWTH Aachen University, 52064 Aachen, Germany*

† Electronic supplementary information (ESI) available. See DOI: https://doi.org/10.1039/d5ee00415b

8104 | *Energy Environ. Sci.,* 2025, **18**, 8104–8129

This journal is © The Royal Society of Chemistry 2025

1. Introduction

Batteries are ascribed a key role in the shift away from fossil fuels to a sustainable and renewable energy system. Assuming the middle of the road shared socioeconomic pathway (SSP2),[1] which presumes medium challenges to climate change mitigation and adaptation, in 2040, an annual battery demand of 5–8 TWh is forecasted, only for electric vehicles (EVs).[2–4] Lithium-ion batteries (LIBs) are the dominant technology across multiple applications, including EVs, portable electronics and stationary energy storage systems (ESS). Global LIB production capacity is approaching 1 TWh annually. The success of LIBs is based on their high energy density, good cycle life and a considerable cost decrease in the last decade to below 100 \$ kWh^{-1}_{cell}.[5–7] As of march 2025, the prices of $LiNi_xMn_yCo_zO_2$ with $x + y + z = 1$ (NMC) and $LiFePO_4$ (LFP) prismatic cells are as low as 61 and 47 \$ kWh^{-1}, respectively.[8] However, the LIB technology still faces several challenges regarding resource availability, material costs, safety and sustainability.[9,10]

Sodium-ion batteries (SIBs) are a rising post-LIB technology, especially due to their low-cost, abundant and geographically distributed raw materials.[11–13] Despite their relatively brief history, SIBs demonstrate high market maturity, with several players pursuing plans for gigafactory-scale production.[14,15] This is largely rooted in the existence of numerous parallels between SIBs and LIBs. Both share the same "rocking chair" working principle, and in addition SIBs are considered a "drop-in" technology enabling production with current LIB gigafactory machinery.[16]

Nevertheless, there are specific distinctions between the technologies, originating from the electrochemical properties of Li and Na. The often-named differences in their ionic radii (Li: 0.76 Å, Na: 1.02 Å), molar mass (Li: 6.9 g mol^{-1}, Na: 23.0 g mol^{-1}) and standard electrode potential (Li: −3.02 V, Na: −2.71 V) are cited as reasons for SIBs not being able to reach competitive energy densities.[17] Further contributing to this argument is the fact that Na is the only alkali metal, which shows no appreciable intercalation into graphite, due to the thermodynamic instability of binary graphite intercalation compounds.[18–22] As a consequence, hard carbon (HC), a low-cost anode active material (AAM) with moderate capacity, has been widely researched and is state of the art (SOTA) for SIBs.[23–26]

However, the number of Na-based compounds and material classes suitable for use as cathode active materials (CAMs) is considerably greater than that for LIBs. This allows for a more precise tuning of CAM properties, which could pave the way towards competitive SIB cells given that cell voltage as well as capacity, are largely dependent on the CAM.[27,28] Furthermore, the elevated standard electrode potential allows for the application of Al as an anode current collector, thereby eliminating Cu from the cell. This enables safe cell transport at 0 V as well as reduced weight, cost and environmental footprint.[29,30]

To evaluate the technology and market readiness level (TRL and MRL) of SIBs, key performance indicators – especially cycling performance, safety, cost, energy density, and sustainability – must be assessed and benchmarked against SOTA LIBs.

The cycle life and safety of SIBs are highly dependent on the specific cell chemistry.[31,32] In particular, polyanionic-type materials, but also SIBs based on Prussian blue analogues (PBAs), demonstrate excellent cycling stability and good safety characteristics, as reflected in analyses of initial commercial cells.[33,34] In contrast, layered oxide-based SIBs generally exhibit a shorter cycle life compared to LIBs,[35] and represent the SIB-CAM group most prone to thermal runaway.[36] Additional real-world data on safety and cycling performance are required for a robust evaluation of TRL and MRL.

A recent study by Yao et al.[37] modeled SIB cost trajectories against LFP/graphite across >6000 scenarios, simulating varying supply chain conditions, raw material prices and learning rates. The study indicates that SIBs could reach cost parity with LFP cells in the 2030s, especially in scenarios with increased Li and/or graphite prices. However, the authors emphasize that increasing the material and cell energy density of SIBs is the biggest factor towards cost competitiveness, on a \$ kWh^{-1} basis.

Despite its central role in both cost and technological competitiveness, comprehensive assessments of the energy density of SIBs remain scarce and limited to the lab-scale.[38] A similar gap is observed for studies on sustainability and carbon footprint (CF) (see Section 2.2). Currently, the sustainability of battery cells is primarily associated with derisking supply chains and reducing the use of toxic and scarce elements (e.g. Co).[39,40] However, in the near-future, especially the CF of batteries is expected to increasingly influence cell costs and market access due to rising carbon prices[41] and the implementation of stricter regulations.[42,43]

Consequently, this work aims to close these research gaps by benchmarking commercially promising SIB chemistries, in terms of specific energy, energy density and CF in large-format cells and a GWh $year^{-1}$ production environment. The aim is to provide a quantitative assessment in the often just qualitative discussion. The analysis focuses on commercially relevant materials since they are the best indicator for the development stage of SIBs. An LFP/graphite-based LIB is used as a point of comparison, given that it can be regarded as the primary competing technology for SIBs in terms of energy density and cost. First, an overview of the electrochemical properties of commercially pursued SIB active materials is given. The obtained cell chemistries are then modeled in comprehensive cell energy density calculations, additionally analyzing the impact of cell format (pouch and prismatic) and electrode coating thickness. Subsequently, the modeled cell designs are transferred into a gigafactory-scale production model utilizing primary machine data and gigafactory layout planning, quantifying energy consumption and material use on a GWh $year^{-1}$ production basis. The output of the cell and production model serve as input for the cradle-to-gate life cycle assessment (LCA). The active material synthesis is modeled based on large-scale industry data, including processing materials, which, to our knowledge, is unprecedented for Na layered oxide and polyanionic SIB-CAMs. Moreover, new life cycle inventory (LCI) data are provided for large-scale synthetic graphite and HC synthesis. A novel modeling approach, for

This journal is © The Royal Society of Chemistry 2025

Energy Environ. Sci., 2025, 18, 8104–8129 | 8105

the first time, quantified emerging volatiles as an energy source for AAM synthesis, enabling a systematic comparison between synthetic graphite and HC, as well as across different HC precursors. The final output is the cradle-to-gate CF of LFP/graphite and selected, commercially relevant SIB cell chemistries. In a detailed breakdown, the impacts of the various cell materials and stages of cell production are differentiated to identify emission hotspots. In scenario analyses, the impact of applying electrochemically advanced HC is examined, as well as the switch from NMP to water-based cathode processing.

2. Review of SOTA SIBs

2.1 Commercially pursued SIB active materials

The LIB market is consolidated on a limited number of cell chemistries. As CAMs in EVs, Ni-rich layered transition metal oxides (NMC and $LiNi_xCo_yAl_zO_2$ (NCA)) for high energy cells and low-cost LFP are dominating.[44] Graphite remains the predominant AAM, and in recent years has been increasingly coupled with small amounts of Si (< 10 wt%) to form Si/C composites.[45–49] The combination of high energy density and high cost makes Ni-rich CAMs paired with Si/C anodes a rather complementary technology to SIBs.[50] In contrast, LFP/graphite cells exhibit performance metrics comparable to SIBs, thus were selected as a reference in this study.

Contrastingly, for SIBs, there is still a big uncertainty about which cell chemistries can overtake considerable market shares. Especially the question of which CAM can best balance performance, safety, resource availability and cost is not decided yet. In academic literature, countless numbers of active materials are researched. However, few have yet made it into a commercial product on a considerable scale.[17] Most SIB-CAMs can be classified within the three overarching classes of layered oxides, polyanionic-type materials and PBAs.

As an AAM, HC[51–54] is the dominating material, but also other carbon-based anodes like soft carbon[55,56] and even graphite[18–22] are investigated. Additionally, alloying materials (Ge, Bi, Sn, Si and P) and conversion-type anodes (e.g. MoS_2, SnS_2) are subject to investigation due to their high theoretical capacities (Sn: 847 mAh g^{-1}, P: 2596 mAh g^{-1}).[57–59] However, they are still far from commercial application, mostly rooting from high volume changes or low electronic conductivity resulting in poor cycling stability, low initial coulombic efficiency (35–90%) or low-rate capabilities. Considering the objective of this study to analyze scalable and commercially viable SIB cell chemistries towards a GWh year^{-1} production volume, materials with a low TRL and MRL have been excluded from the analysis.

2.1.1 SIB cathode active materials. Table 1 gives an overview of the CAMs that are applied or researched by key SIB cell manufacturers and CAM producers. The observed companies were chosen based on recent market reviews,[14,15,60,61] and the electrochemical data were collected from publications, patents and company announcements. The listed CAMs are selected exemplary based on their performance data.

Layered oxides currently represent the most utilized class of CAMs for LIBs and are also pursued by numerous SIB cell manufacturers. The British company Faradion applies Ni and Mn-based materials, which are doped with Mg and Ti (NMMT). Their Gen1 material, O3-NMMT, reached 157 mAh g^{-1} of cathodic capacity in a full cell with HC.[29] However, the cycling stability was not competitive with LIB-CAMs. Switching from an O3-structure to biphasic P2/O3-NMMT in Gen2 led to a distinctly increased cycle life while reaching similar capacities. The Chinese manufacturer HiNa utilizes O3-type layered oxides mainly formed out of Cu, Fe and Mn. The exact stoichiometry and the addition of further dopant elements differ between publications and patents.[62–64] The French company Tiamat recently announced the development of a Gen2 cell targeting the EV and ESS market, which employs a layered oxide CAM.[65] Among others, $O3-NaNi_{0.45}Zn_{0.05}Mn_{0.4}Ti_{0.1}O_2$ (O3-ZNMT) was presented as a potential CAM by the company. The CAM was synthesized in the research group of Jean-Marie Tarascon, shareholder and part of the development committee of Tiamat, delivering 171 mAh g^{-1} in a half-cell at a cut-off of 4.5 V.[66,67] Recently, the first cell characterizations of commercial SIBs were published. The cells generally stem from China and entail $O3-NaNi_xFe_yMn_zO_2$ (O3-NFM) as the CAM.[68–72] O3-NFM occurs in various stoichiometries, comparable to Li-NMC. Furthermore, various doping elements (Zn, Ti, Cu, ...) can be added. Additionally, the commercial relevance of O3-NFM is underlined by the fact that the world's largest NMC producer, Ningbo Ronbay,[73] holds several patents covering O3-NFM synthesis (and closely related chemistries).[74–79] Other industrial CAM producers like BTR are already publicly advertising O3-NFM.[80] The announcement of CATL, the world's largest LIB cell manufacturer, in 2021 to industrialize SIBs by 2023 received broad public attention worldwide. Initially, CATL only announced plans to develop PBAs. However, their intellectual property (IP) portfolio and the high specific energy (175 Wh kg^{-1}) of their recently announced SIB "Naxtra"[81] also suggest the use and development of layered oxides, especially O3-NFM-related CAMs.[82–85] The practical capacities reached in Ronbays and CATL's patents are generally in the range of 140–170 mAh g^{-1}, depending on the exact chemistry and cutoff voltage, which is consistent with academic data (Table 1). Chinese manufacturers have already established ton-scale production of O3-type layered oxides.[86]

Tiamat's first generation of high-power SIB cells was based on the polyanionic CAM $Na_3V_2(PO_4)_2F_3$ (NVPF). Table 1 contains cycling data of a recent evaluation of a Tiamat 2020 prototype 18 650-type cylindrical cell, as well as data from selected publications for comparison. Noticeable is the higher average discharge voltage (~ 3.85 V) and the superior cycling stability compared to the layered oxides, making NVPF a promising candidate for use in commercial cells. Recently, the polyanionic compounds $Na_4Fe_3(PO_4)_2(P_2O_7)$ (NFPP) and alluaudite $Na_{2+2x}Fe_{2-x}(SO_4)_3$ ($x \leq 0.3$) (NFS) have gained momentum due to their low cost and high cycling stability. Currently, their production is carried out almost exclusively in China. The first commercially available NFPP materials[87–89]

8106 | Energy Environ. Sci., 2025, **18**, 8104–8129

This journal is © The Royal Society of Chemistry 2025

Table 1 Overview of the key electrochemical parameters of SOTA CAMs pursued by selected SIB cell manufacturers and CAM producers

CAM	Company	Reversible capacity in half-cell [mAh g⁻¹] 0.1C	1C	Reversible capacity in full cell vs. HC [mAh g⁻¹]	Average discharge potential vs. Na/Na⁺ [V]	Upper cutoff volt. [V]	Cryst. density [g cm⁻³]	ΔV_{charge} [%]	Capacity retention, cycle number, rate – half-cell	Capacity retention, cycle number, rate – full cell vs. HC	Ref.
Layered oxides											
O3-NMMT[a]	Faradion Gen1	—	—	157 (C/15)	3.16	4.2	4.17	—	—	~80%, 200, C/6	29, 124 and 125
P2/O3-NMMT[b]	Faradion Gen2	147 (0.2C)	—	130 (C/10)	3.15 vs. HC	4.2	4.18	Claim: "small"	—	80%, 1000, 1C	29 and 126
		—		—	3.32	4.25				—	
		156 (0.2C)		154 (C/7)	3.2 vs. HC	4.3				—	
		—		—	3.34	4.35				—	
O3-CFM[c]	HiNa	102	78	85.7 (0.5C)	3.2 vs. HC	4.05	4.41	—	97%, 100, 0.1C	~99%, 100, 0.5C	62 and 63
O3-CNFM-CT[d]	HiNa patent	125.6 (0.2C)	107.3	—	—	4.0	4.50	—	66%, 100, 1C	—	64
O3-CNFM-WZ[e]	HiNa patent	131.6 (0.2C)	115.7	—	—	4.0	4.49	—	75%, 100, 1C	—	64
O3-NFMT[f]	CATL patent	132	—	—	—	4.2	4.15	—	94.2%, 100, 1C	—	82
		164	—	—	—	4.5		—	81.6%, 100, 1C		
O3-ZNMT[g]	Academic data pot. Tiamat Gen2	—	—	152 (0.1C)	3.31	4.4	4.53	→P3: −10[g] (4.5 V)	—	82%, 100, 0.1C	38 and 66
O3-NFM111[h]	Ningbo Ronbay patent	171	—	—	~3.3[145]	4.5	4.51	—	—	—	76
O3-NFM424[i]	Academic data	133	112	161 (0.1C)	~3.1	4.3	4.54	0[142]/+2[128] (4.0 V)	96.4%, 30, 0.05C	88.5%, 600, 0.1C	127 and 128
		165 (0.05)	—		~3.3	4.0		11 (4.2 V)			
Polyanionic-type											
NVPF[j]	Tiamat Gen1 prototype 2020	128	—	68 Wh kg_cell⁻¹ (1C)	3.7 vs. HC	4.25	3.16	−3 (4.5 V)	—	80%, 1600, 5C	33
	Academic data	133 (0.5)[129]	129	—	3.8	4.3	3.16	−3 (4.5 V)	93%, 100, 1C	—	129-132
		138 (0.5)[130]	134	—	3.85	4.5			86.4%, 300, 1C	—	
				100[131]	3.4 vs. HC	4.3				80%, 3800, 1C	
NFPP[k]	Jiana Energy patent	123	98.5 (5C)	—	—	—	3.29	−4[143]	99.1%, 1000, 1C	—	90
	Ningbo Ronaby patent	127.8	—	—	~3.2	4.0		—	~93%, 70, 1C	—	91
NFS[l]	Zoolnasm patent	110.2	—	—	~3.3	4.5	3.11	−1.6[144]	95.0%, 1000, 5C	—	97
Prussian blue analogues											
Fe-PBA[m]	Altris/Northvolt Claims & patent	Claim: 160 Patent: 140	—	Claim: 160 Wh kg_cell⁻¹	~3.2	4.2	2.21	+13 (4.0 V)	—	—	106, 107, 133 and 134
Fe-PBA[n]	Academic data	157	145 (10C)	119 (0.08C)	~3.2	4.2	2.21	+13 (4.0 V)	80%, 750, 0.5C ch.	—	135
Mn-PBA[o]	CATL patent	160	—	Claim: 160 Wh kg_cell⁻¹	~3.5	4.0	2.20	+13[r]	—	94%, 50, 10 mA g⁻¹	136-140
Mn-PBA[p]	Academic data	—	—	140 (0.7C)	3.5	3.8	2.13	+13[r]	—	~99%, 30, 0.7C	141
		150	148	—		4.0			75%, 500, 0.7C	—	

[a] O3-Na$_{0.95}$Ni$_{0.317}$Mn$_{0.317}$Mg$_{0.158}$Ti$_{0.208}$O$_2$. [b] 1/3: P2-Na$_{0.667}$Ni$_{0.300}$Mn$_{0.600}$Mg$_{0.033}$Ti$_{0.067}$O$_2$ + 2/3: O3-NaNi$_{0.333}$Mn$_{0.333}$Mg$_{0.167}$Ti$_{0.167}$O$_2$. [c] O3-Na$_{0.9}$Cu$_{0.22}$Fe$_{0.3}$Mn$_{0.48}$O$_2$. [d] O3-Na$_{1.0}$Cu$_{0.15}$Ni$_{0.2}$Fe$_{0.3}$Mn$_{0.33}$O$_2$ sintered with CuO and TiSO$_4$ to form a coated CAM. [e] O3-Na$_{0.9}$Cu$_{0.15}$Ni$_{0.18}$Fe$_{0.3}$W$_{0.01}$Mn$_{0.34}$O$_2$ sintered with WO$_3$ and Zr(NO$_3$)$_4$ to form a coated CAM. [f] O3-Na$_{0.85}$Ni$_{0.175}$Fe$_{0.2}$Mn$_{0.525}$Ti$_{0.05}$O$_2$. [g] O3-NaNi$_{0.45}$Zn$_{0.05}$Mn$_{0.4}$Ti$_{0.1}$O$_2$. [h] Na$_{1.0}$Ni$_{0.33}$Fe$_{0.33}$Mn$_{0.33}$O$_2$. [i] O3-NaNi$_{0.4}$Fe$_{0.2}$Mn$_{0.4}$O$_2$. [j] Na$_3$V$_2$(PO$_4$)$_2$F$_3$. [k] Na$_4$Fe$_3$(PO$_4$)$_2$(P$_2$O$_7$). [l] Alluaudite Na$_{2+2x}$Fe$_{2-x}$(SO$_4$)$_3$ ($x \leq 0.3$). [m] Na$_{2-x}$Fe[Fe(CN)$_6$]. [n] R-Na$_{1.92}$Fe[Fe(CN)$_6$]. [o] Na$_2$Mn[Fe(CN)$_6$]. [p] Na$_{1.89}$Mn[Fe(CN)$_6$]$_{0.97}$. [q] At 4.5 V the crystal consists of P3 and O1 domains, but the P3 structure prevails. [r] For complete desodation (Na = 0). For partial desodation (Na = 0). ΔV = 27%.

This journal is © The Royal Society of Chemistry 2025

Energy Environ. Sci., 2025, **18**, 8104–8129 | **8107**

delivered specific capacities of $\sim$100–115 mAh g^{-1}. However, both company patents[90,91] and academic work[92] indicate that values near the theoretical capacity of 129 mAh g^{-1} can be reached and even exceeded through elemental doping.[93,94] NFS offers the advantage of a high nominal voltage ($\sim$3.8 V), but its theoretical capacity of 120 mAh g^{-1} has not been reached. Commercial NFS CAMs typically show capacities $<$100 mAh g^{-1}.[95,96] A practical capacity of $\sim$110 mAh g^{-1} represents the highest reported value in company patents[97] and academic studies.[98,99] Mass production lines for both NFPP and NFS have recently become operational. NFPP manufacturing sites, in particular, are being scaled up to production volumes comparable to those of LIB-CAMs, with sites reaching $\geq$10 000 mt of annual output.[86,100] Major producers include Jiana Energy Technology,[90,101] Ningbo Ronbay[102] and BYD's technology partner Zhejiang NaTRIUM Energy.[103] Moreover, Chinese cell manufactures like BYD[104] and Zoolnasm[105] (or Zhongna) are pursuing GWh-scale production of NFPP/HC and NFS/HC cells, respectively. Although NFPP and NFS cell prices are already competitive to LFP-based LIBs, their lower energy density currently limits their application to ESS and micro-mobility applications.[86]

In the CAM class of PBAs, two different materials are currently pursued by cell manufacturers. The Swedish cell manufacturer Northvolt announced that they developed a SIB cell based on a Na$_{2-x}$Fe[Fe(CN)$_6$] (Fe-PBA) CAM with their research partner Altris, reaching a specific energy above 160 Wh kg^{-1} at the pouch cell level.[106] While their filed patent only shows a reversible half-cell capacity of 140 mAh g^{-1}, Altris claims to reach 160 mAh g^{-1} with their Fe-PBA material.[107] CATL is working on Na$_2$Mn[Fe(CN)$_6$] (Mn-PBA). Similar to Northvolt, they claim to have reached 160 Wh kg^{-1} at the cell level. Since both cell manufacturers did not publish comprehensive electrochemical data, academic data are listed in Table 1 for comparison.

Fig. 1 illustrates the cathodic specific energy [Wh kg^{-1}] and energy density [Wh L^{-1}] of the materials described. It is noteworthy that SIB-CAMs from all three material classes reach comparable ($\pm$10%) specific energies to LFP, shown for reference in green, while several layered oxides achieve even higher energy densities. PBAs are competitive in terms of specific energy, but since their crystallographic density ($\sim$2.2 g cm^{-3}) is halved compared to the layered oxides (4.1–4.5 g cm^{-3}), they only reach about half their energy density. The most promising CAMs regarding energy density are the Ni-based layered oxides O3-ZNMT and O3-NFM111/424, which exceed the volumetric energy density of LFP by 24–37%.

2.1.2 SIB anode active materials. For SIB cell manufacturers, the CAM is mostly a very important part of their IP and often patent protected. Hence, a wide variety of CAMs are observable on the SIB market. Regarding the AAM, the situation is different. HC is, by far, the most widely used material and is applied by nearly all cell manufacturers. The fact that all published teardowns of commercial SIB cells identify HC as the AAM reinforces the absence of competitive alternatives to HC in the market.[68–72] The only notable exception is the high-power cell from Natron Energy, which utilizes two different PBA materials as the AAM and CAM.[34] Given its significantly lower
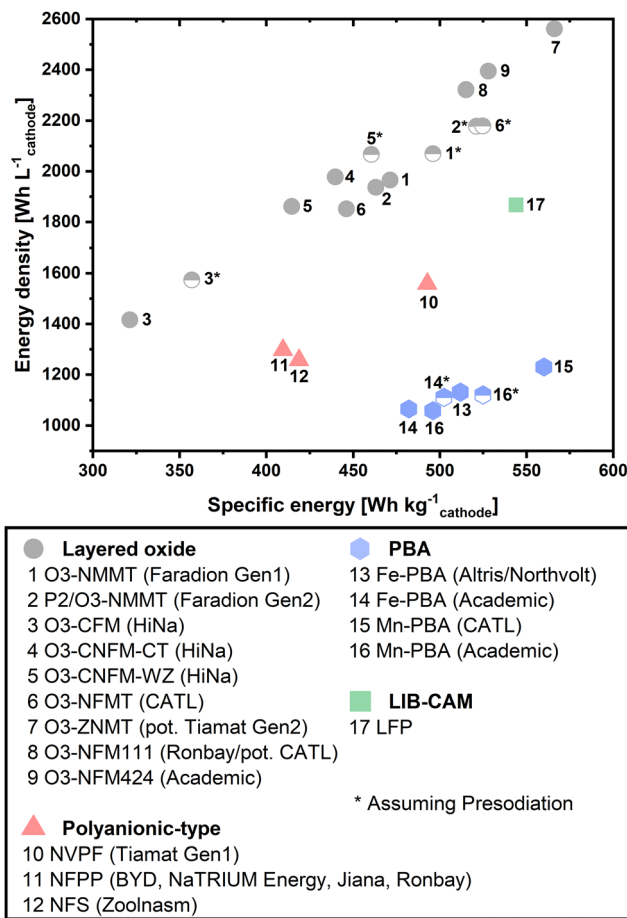

Fig. 1 Specific energy and energy density of the material-level of SIB-CAMs pursued by SIB cell manufacturers in comparison to LFP. The underlying data are listed in Table S2 (ESI†).

energy density and distinct application scope, this cell chemistry was excluded from the scope of this study.

While CATL, Faradion and HiNa also investigate and develop in-house HC materials, there is a rising number of material manufacturers producing HC active materials. With increasing market shares of SIBs, a similar development to the LIB-AAM graphite can be anticipated, which is now a commodity purchased by cell manufacturers from graphite producers. This is reinforced by the fact that several of the largest graphite producers,[73] among others BTR, Shanshan and Shanghai Putailai, already started ramping up HC production.

Table 2 lists electrochemical data for HC produced by relevant cell and material manufacturers operating at pilot- or mass-production scale. The companies were selected based on the HC market analysis of Liu et al.[108] and further research. The material data provided in Table 2 were taken from publications, patents and company websites, providing an insight into the industry's status quo. The claimed capacities show large variations, but most are in the range of 300–350 mAh g^{-1}. The initial coulombic efficiency, which remains a challenge in HC development,[109,110] lies predominantly in the range of 88 $\pm$ 4%.

HC can be produced from a wide variety of carbonaceous precursors, which is also visible in industrial production. The

8108 | *Energy Environ. Sci.*, 2025, **18**, 8104–8129

This journal is © The Royal Society of Chemistry 2025

Table 2 Overview of the electrochemical parameters of SOTA AAMs pursued by selected SIB cell manufacturers and AAM producers. SSA = specific surface area, CVD = chemical vapor deposition

AAM	Country	Company, product name	Precursor material	Claimed rev. capacity [mAh g^{-1}]	Tap density [g cm^{-3}]	SSA [m^2 g^{-1}]	Particle size (D50) [µm]	Initial coulombic efficiency [%]	Ref.
HC	UK	Faradion	—	330	—	—	—	91.9, 0.05C, half-cell; 90, 0.1C, full cell	29
	China	CATL	—	350	—	—	—	—	137
	China	Hina patent	Coal-tar, petroleum or natural pitch	301.2	—	—	0.5–3	88.6	146
	Japan	JFE Chemical	Coal-tar pitch	350–410 (LIB)	—	0.7–5.0	—	—	147 and 148
	China	Tianjin Yufeng Carbon	Coal pitch	280–450 (SIB & LIB)	—	—	—	80–85	149 and 150
	Japan	Sumitomo Bakelite	Phenolic resin (calixarene based)	320 (0.05C)	—	—	—	—	151
	China	Wuhan Bixidi Battery Material	Resin based	—	—	—	—	—	152
	Japan	AT Electrode, Bellefine – LN-0005	Phenolic resin	200–300 (0.1C, LIB)	0.8 ± 0.15	<10	5.0 ± 2.0	—	153
	Japan	AT Electrode, Bellefine – LN-0001	Phenolic resin	305.27	0.78 ± 0.15	<30	1.5 ± 0.5	72.92, half-cell	153 and 154
	China	Shengquan Group, SQNHC-001	Bio-based resin	290 ± 5	0.93 ± 0.2	≤5	4–7	≥91	155
	China	Shengquan Group, SQNHC-002	Bio-based resin	320 ± 5	0.95 ± 0.2	≤5	4–7	≥92	155
	China	Shengquan Group, SQNHC-003	Bio-based resin	350 ± 5	0.95 ± 0.2	≤5	4–7	≥92	155
	Japan	Kuraray, Kuranode-Type 2	Coconut shell charcoal	298 (0.1 mA cm^{-2})	—	6/4	5/9	90	156 and 157
	Sri Lanka	Haycarb, HCH102	Coconut shell charcoal	300	0.75	<10	7–9	90	158
	Finland	Stora Enso	Wood lignin	—	—	—	—	—	159
	Estonia	UP Catalyst, Catasol A400	Lignin	250–300	—	<10	12 (D90)	99.8 (3rd cycle)	160
	China	BTR, BSHC-260	"Plant based"	260 ± 5	0.9 ± 0.1	≤5.0	6.0 ± 1.5	≥88.0	161
	China	BTR, BSHC-300	"Plant based"	295 ± 5	0.8 ± 0.1	≤5.0	6.0 ± 1.5	≥88.0	161
	China	Xiangfenghua (XFH) patent	Shell (e.g. coconut)[163] Coal[165]	334–346 (CVD) 238–266	—	1267–1454	—	92.8–94.3 84.3–87.0	162–165
	China	Hina patent	Bituminous coal	342.0	0.8	—	—	86.1	166
			Bamboo	384.0	0.70			85.7	
			Coconut shell	329.0	0.61			89.0	
			Petroleum coke	315.0	0.90			82.4	
	China	Shanshan	Various: biomass-, asphalt-, resin-based	350	0.70–0.90	<9	5–10	—	167 and 168
	S. Korea	Aekyung Chemical, PAC-2	—	275 ± 15	≥0.8	3.6 ± 0.7	8.0 ± 1.0	84 ± 2	169
	China	BEST GRAPHITE (BSG), NHC-330	—	332.5	0.77	3.58	9.25	90.5	170
	China	BEST GRAPHITE (BSG), YHC-1	—	294.6	0.65	5.27	9.1	89.2	171
	China	Shinzoom	—	523.1 (LIB)	0.89	1.87	15.66	≥73.67 (LIB)	172
	China	Shanghai Putailai (Jiangxi Zichen), P55	—	—	—	—	—	—	173
Soft carbon	China	Hina	Anthracite	222	—	3.55	1–10	81	174
Carbon composite	China	Hina patents	Coal powder + asphalt (80:20)[175]	271.4	1.03	—	8.2	83.0	175 and 176
			Coal powder + needle coke (80:20)[175]	264.5	1.12	—	8.78	83.7	
			Iron charcoal + petrol. asphalt (40:1)[176]	304.9	—	—	—	90.79	

This journal is © The Royal Society of Chemistry 2025

Energy Environ. Sci., 2025, 18, 8104–8129 | 8109

most common precursors are (phenolic) resin, biomass materials (especially coconut shells and lignin) and pitches (from petroleum or coal-tar), which align well with the analysis of Liu et al.[108] It can be concluded that several precursors are possible for scaled and cost-competitive HC production, and none are yet prevailing. The data in Table 2 do not permit statistical inference regarding the impact of precursor choice on the electrochemical performance of the respective HC. Nevertheless, the importance of precursor selection is reinforced not only in various studies,[29,111–114] but also by the fact that many companies do not disclose the underlying precursors for their HC material. Moreover, other factors such as the pre-treatment method[115–117] or the pyrolysis conditions[118–120] have a substantial impact on the final electrochemical performance of HC. Differences in precursor choice and synthesis conditions lead to significant variations in the electrochemical performance of commercial HCs, highlighting considerable potential for optimization.

2.2 LCA studies on SIBs

To evaluate the environmental competitiveness of battery cells, LCA has emerged as a scientific ISO-normed method to quantify environmental impacts.[121] In contrast to numerous LCA studies on LIBs, so far only a limited number of studies examine the environmental impact of SIBs, due to their early stage of development. In a first approximation, for SIB production, a higher material and energy demand per kWh of cell energy can be assumed, mainly due to the lower energy density of SIBs compared to LIBs. Therefore, existing studies were screened not only for the CF of SIB cells but also for the associated cell energy density. Furthermore, the occurrence of industrial-scale material synthesis and production data is reviewed.

Peters et al.[122] were amongst the first to conduct an LCA study about the environmental performance of a layered oxide NMMT battery with HC derived from sugar. In their study, the SIB with an energy density of 128 Wh kg^{-1} led to a cradle-to-gate impact of 140 kg CO_2-eq. kWh^{-1}.

Schneider et al.[123] conducted a cradle-to-gate LCA of a NaNMC/HC battery, which reached 120–152 Wh kg^{-1} and 80–150 kg CO_2-eq. kWh^{-1} depending on C-rate. The energy consumption for battery cell production made up 20–37% of the global warming potential (GWP).

In 2021, Peters et al.[30] presented the most comprehensive LCA on various SIB cell chemistries. The variants include HC paired with NMMT (171.9 Wh kg^{-1}, 50.6 kg CO_2-eq. kWh^{-1}), $Na_{2/3}Mn_{0.95}Mg_{0.05}O_2$ (NaMM) (157.1 Wh kg^{-1}, 52.3 kg CO_2-eq. kWh^{-1}), $Na_{1.05}(Ni_{0.33}Mn_{0.33}Co_{0.33})_{0.95}O_2$ (136.3 Wh kg^{-1}, 86.7 kg CO_2-eq. kWh^{-1}), Fe-PBA (124.1 Wh kg^{-1}, 87.0 kg CO_2-eq. kWh^{-1}), and $Na_4MnV(PO_4)_3$ (152.5 Wh kg^{-1}, 89.7 kg CO_2-eq. kWh^{-1}), from which only NMMT and Fe-PBA are of commercial relevance, based on the industry review in Section 2.1.1.

All analyzed SIB cells exhibited lower specific energy and higher cradle-to-gate GWP compared to LIBs, namely NMC622/graphite (272 Wh kg^{-1}, 44.8 kg CO_2-eq. kWh^{-1}) and LFP/graphite (197 Wh kg^{-1}, 49.6 kg CO_2-eq. kWh^{-1}). However, different to previous studies, specific SIB cell chemistries (NMMT and NaMM) achieved comparable GWPs to LIBs due to a nearly competitive energy density and omitting or limiting cobalt and nickel content. CAM production and the energy demand during cell production were identified as greenhouse gas (GHG) emission hotspots, each making up 30–50% of the GWP, depending on cell chemistry. Even though the authors claimed to model prismatic cells, the weight of the cell housing suggests that a pouch format was assumed. An LCA of large prismatic SIB cells is still missing in the literature. Besides the cradle-to-gate impacts, the authors, for the first time, performed a cradle-to-grave assessment of SIB cells, also including use-phase and end-of-life, i.e. recycling of the battery.

All described studies assumed active material synthesis routes based on typical laboratory precursors and conditions, due to a lack of industrial data. In a recent study Wickerts et al.[177] were the first to provide LCI data for industrial synthesis of Fe-PBA, obtained from a material manufacturer.

Further scientific studies specifically examined the CAM or AAM synthesis of SIBs. Baumann et al.[178] screened 42 different SIB CAMs, among others regarding CF, providing a broad overview. However, the modeled synthesis is very simplified, focusing on the CAM elemental composition and not on the actual precursors that are applied in scaled production. Moreover, no processing chemicals were considered.

Regarding the AAM, Peters et al.[179] did a thorough LCA of HC synthesis from waste tires, apple pomace and phenolic resin, also considering gas and tar volatiles emerging during pyrolysis. However, the gas and tar yield are lacking a profound data basis and their molecular composition was not further considered. Liu et al.[180] investigated the HC synthesis from four different precursors. Based on primary laboratory values, the HC production from coconut shells and bamboo waste was examined, using an LCA approach. Secondary data for HC derived from apple pomace and waste tires were taken for comparison. The results revealed large differences in emissions, with HC synthesized from bamboo waste exhibiting the highest GWP (8.80 kg CO_2-eq. kg$^{-1}_{HC}$), while HC derived from coconut shells performed the best (0.39 kg CO_2-eq. kg$^{-1}_{HC}$).

In the absence of industrial primary data, Liu et al.[181] employed a simplified scale-up approach and a predictive LCA to estimate the CF of industrial-scale HC synthesis. By scaling up a laboratory process, they calculated a CF of 3.6 kg CO_2-eq. kg$^{-1}_{HC}$ for industrial HC production from bamboo. In a best-case scenario, the CF could be reduced to 0.4 kg CO_2-eq. kg$^{-1}_{HC}$. This scenario included, among other factors, the combustion of emerging volatiles, although the associated energy recovery was estimated rather than explicitly calculated.

The review of LCA studies analyzing SIBs reveals that, while many cell components and chemistries have already been investigated, the data basis is still limited compared to LIBs, leaving several research gaps. Regarding CAM synthesis, only Wickerts et al. modeled Fe-PBA synthesis on an industrial-scale. For Na layered oxides and polyanionic-type CAMs no comprehensive LCI data for scaled synthesis can be found in the literature. On the anode side, HC synthesis from different precursors has been investigated, however often looking at industrially irrelevant precursors and/or not comprehensively accounting for the energy produced by emerging volatile

8110 | Energy Environ. Sci., 2025, 18, 8104–8129

This journal is © The Royal Society of Chemistry 2025

combustion. The latter has significant impact on the energy balance of the synthesis, which also applies for graphite synthesis for LIBs as further elaborated in Section S3.3.1 of the ESI.† The cradle-to-gate GWP has been calculated for several cell chemistries. However, several commercially relevant CAMs (Table 1) have not been investigated yet. Furthermore, the CF of cell production varies largely between studies and lacks a profound data basis.

This analysis aims to narrow and close several of these research gaps, especially focusing on industrial-scale SIB production. First, LCI data for large-scale synthesis of Na layered oxides and polyanionic-type CAMs are provided. Second, an in-depth, quantitative mass and energy assessment of the volatiles arising in the synthesis of HC and the synthetic graphite precursor needle coke is performed, resulting in a new LCI dataset for industrial graphite and HC production. By applying this method, HC synthesis is investigated for four different, industrially relevant precursors. Third, for the first time, large-scale prismatic SIB cells, comprising commercially pursued active materials are modeled on a GWh year^{-1} production scale, utilizing primary machine data.

3. Methods

The results of this in-depth analysis are based on linkage of three distinct models, namely a battery cell model, a battery cell production model and an LCA model. An illustration of the models and the research approach is shown in Fig. 2. The basis of all three models is the material input, which is based on the reviewed SIB active materials. The battery cell model defines material input, cell chemistry and cell format. Its output includes the cell's energy density and a bill of materials (BOM) accounting for all materials within the cell. Subsequently, the production model simulates the manufacturing of the defined cell at gigafactory-scale, providing the energy consumption per kWh$_{cell}$ and a second BOM, including the processing materials.

The respective BOMs, the cell energy density and the energy consumption of production are the feedstock for the LCA model. In the following, the different models are explained in further detail.

3.1 Battery cell model

The energy density was calculated for a large-format pouch, as well as prismatic cells based on industrial cell designs. Metrics of cell housing and cell components are listed in Table S1 (ESI†). Table S2 (ESI†) shows the electrochemical data of the active materials applied in the calculations, which were based on Table 1. Since the SIB-AAM HC exhibits varying electrochemical properties (see Table 2), two scenarios were modeled: HC-basic (325 mAh g^{-1}, 0.3 V vs. Na/Na$^+$, 1.5 g cm^{-3}) representing the SOTA and HC-optimized (375 mAh g^{-1}, 0.2 V vs. Na/Na$^+$, 1.8 g cm^{-3}), depicting a near future scenario and reflecting the high potential for optimization of HC. In contrast to graphite and the CAMs, commercial HC is not close to its theoretical capacity and exhibits several notable opportunities to enhance

its electrochemical performance, as already demonstrated on a lab-scale.[182–184] Detailed reasoning for the selected HC parameters is given in the ESI.†

The cathode thickness was fixed at 90 μm representing a high energy application, while the anode thickness was calculated in accordance with a 1.1 N : P ratio (negative to positive electrode capacity ratio). To determine the number of stacks (N_{stacks}) (Fig. S1, ESI†) that fit into the cell housing, the thickness change of the stack during cycling (TC) was considered. N_{stacks} was derived from the interior width of the cell (cw$_{int.}$) and the expanded thickness of a stack ($T_{exp.}$) (1), which results from the uncycled stack thickness ($T_{pristine}$) and TC (2).

$$N_{stacks} = \frac{cw_{int.}}{T_{exp.}} \qquad (1)$$

$$T_{exp.} = T_{pristine} + TC \qquad (2)$$

$$TC = TC_{irrev.} + TC_{rev.} \qquad (3)$$

$$TC_{rev.} = TC_{anode} + TC_{cathode} \qquad (4)$$

$$TC_{anode} = 2 \cdot T_{anode} \cdot \Delta V_{anode} \cdot vol\%_{AAM} \qquad (5)$$

$$TC_{cathode} = 2 \cdot T_{cathode} \cdot \Delta V_{cathode} \cdot vol\%_{CAM} \qquad (6)$$

TC comprises a reversible part (TC$_{rev.}$), originating from active material volume changes during ion de-/intercalation and an irreversible part (TC$_{irrev.}$), due to aging processes,[185] e.g. electrode delamination,[186] SEI formation,[187] Li plating[188] or gas formation[189] (3). Schulze et al.[190] measured an irreversible thickness change of 2.95% for NMC811/graphite prismatic cells, using 2D laser profile sensors on air-compressed cells. Due to a lack of data, especially for SIBs, $T_{irrev.}$ was approximated as 3% of $T_{pristine}$ for all cell chemistries. $T_{rev.}$ (4) consists of the thickness change of the anode (TC$_{anode}$) and cathode (TC$_{cathode}$) which depend on the crystal volume changes of the active materials during charging (ΔV). During lithiation, the graphite structure expands by ∼+10%,[191–193] while the NMC811[194,195] and LFP[195–197] crystals shrink by ∼−3.5% and ∼−6.5% during charging, respectively. HC shows <+5%[198–200] volume expansion during sodiation. The lower volume expansion compared to graphite is rooted in a more porous microstructure of HC, which is reflected in a lower tap density. Crystal volume changes of SIB-CAMs are very material specific, and data availability is limited. Table 1 lists the crystal volume changes of the analyzed CAMs, ranging from significant volume shrinkages e.g. −10% for O3-ZNMT to larger volume increases, e.g. +13% for PBAs. To predict $T_{rev.}$ out of the crystal structure changes of the active materials, the values for TC$_{anode}$ and TC$_{cathode}$ were calculated using eqn (5) and (6), applying a combination of the approaches described by Rieger et al.[201,202] and Ren et al.[195] $T_{anode/cathode}$ is the thickness of the anode/cathode and vol%$_{CAM/AAM}$ is the volume fraction of the respective active material.

The cell capacity (Q_{cell}) is defined by the cathode capacity ($Q_{cathode}$) (7). Due to the considerably lower cost of the anode compared to the cathode, the cell stack was designed to start and end with a double-sided coated anode. This architecture
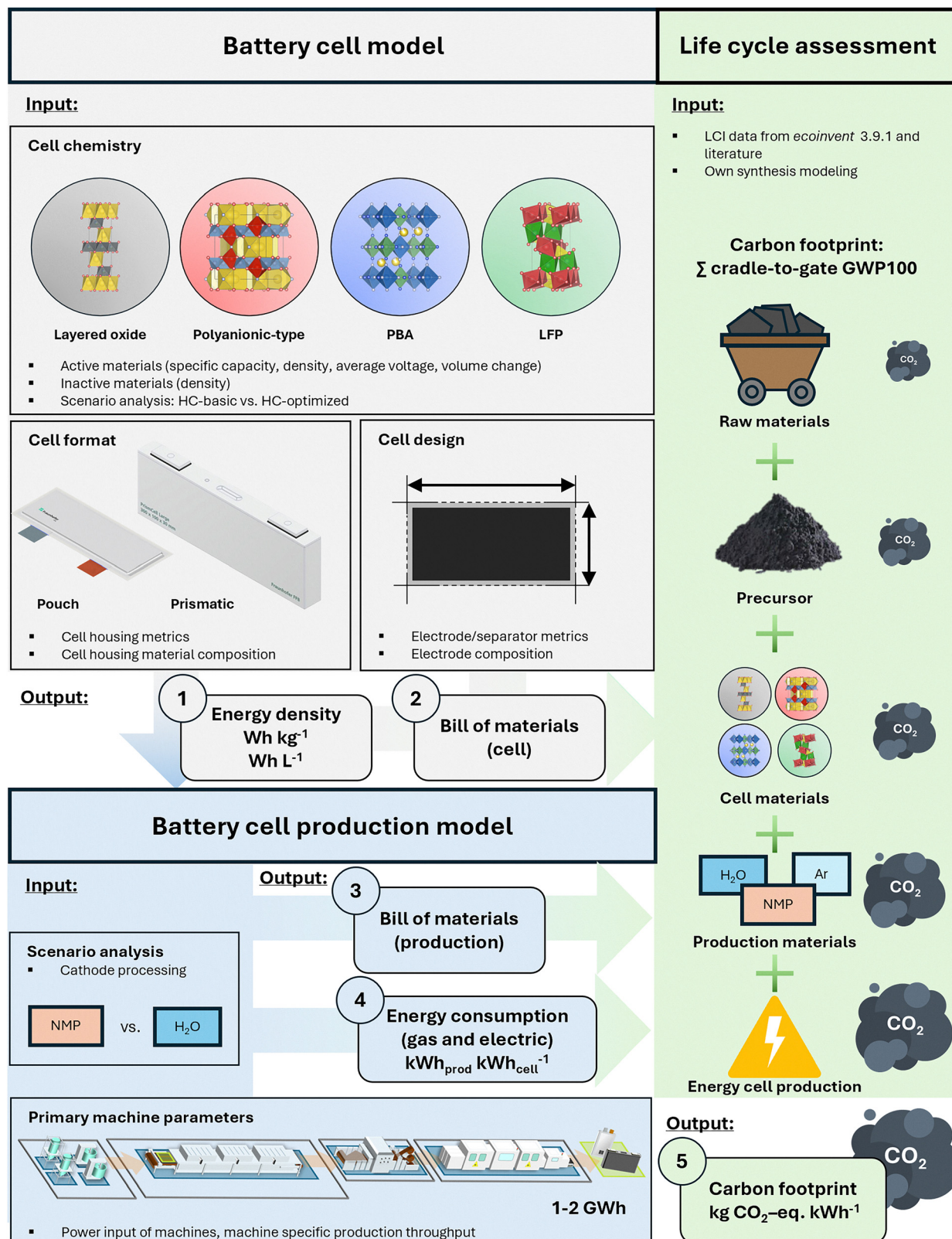
This journal is © The Royal Society of Chemistry 2025

Energy Environ. Sci., 2025, **18**, 8104–8129 | **8111**

Fig. 2 Schematic overview and data flow of the three developed models. The battery cell model calculates the energy density as well as a BOM for the cell, based on material, cell format and cell design input parameters. For the defined cell a GWh year^{-1} production is simulated in the battery cell production model, obtaining BOM and energy consumption values for cell production. The output of these two models, LCI data from ecoinvent 3.9.1, literature data and our own synthesis modeling data, serve as input for the LCA and the calculation of the cradle-to-gate CF. The crystal structure visualizations were created with VESTA 3.90.0a.[205]

8112 | *Energy Environ. Sci.*, 2025, **18**, 8104–8129

This journal is © The Royal Society of Chemistry 2025

avoids the assembly of unused and costly CAM, in line with commercial cell designs.

$$Q_{cell} = (SN_{stacks} - 1) \cdot Q_{cathode} \tag{7}$$

Next to the specific energy and energy density, the result is a BOM, listing the weights of all components that make up the battery cell, not considering scrap in cell production. The detailed equations are presented in the ESI.†

3.2 Battery cell production model

The output of the battery cell model serves as input for the production model, which was based on Degen et al.[2,203] Even though the model was validated for LIB production, SIB technology was assumed as a drop-in technology without major alternations in the production process. The model aims to calculate natural gas and electricity consumption of each production step. The primary data applied for the energy consumption of gigafactory machinery represent average values derived from at least three machine manufactures for each production step.[203] The throughput of the production steps is based on layout planning of the GWh year^{-1} research battery cell factory in Münster, Germany operated by Fraunhofer FFB.[204] Detailed information regarding the data origin can be found in studies by Degen and Schütte[203] and Degen and Krätzig.[204]

In the model, a throughput-based calculation was conducted by calculating the cell specific production throughput ($TP_{j,cell}$) [kWh$_{cell}$ h^{-1}] of each processing step. For the electrode production and cutting steps, $TP_{j,cell}$ is calculated using the product of the producible material flow rate $Q_{j,cell}$ [m^2 h^{-1}] and the areal energy content of the double-sided cathode ($E_{areal.cathode}$) (8). Conversely, for the assembly and finalization processes, $Q_{j,cell}$ [cells h^{-1}] is multiplied with the nominal cell energy (E_{cell}) (9).

$$TP_{j_{electrode},cell} = Q_{j,cell} \cdot 2 \cdot E_{areal.cathode} \tag{8}$$

$$TP_{j_{assembly/finalization},cell} = Q_{j,cell} \cdot E_{cell} \tag{9}$$

For each production step, the machine power is disclosed. The bottleneck of the modeled factory was the assembly line with a throughput of 840 m^2 h^{-1}, hence dictating the output of the whole process chain. For the modeled prismatic LFP/graphite cell, 840 m^2 h^{-1} equal to a throughput of 500 cells h^{-1}, which was set as $Q_{j,cell}$ for the assembly and finalization steps in all scenarios. The energy demand of each machine and production step was normalized to this throughput. In total, the production line has a capacity of ~1–2 GWh year^{-1}, depending on cell chemistry. The result is a cell-specific energy consumption in kWh$_{prod}$ kWh$_{cell}$$^{-1}$ for each production step, distinguishing between gas and electric energy. Furthermore, a BOM for cell production accounts for all processing materials that are not part of the cell, e.g. N-methyl-2-pyrrolidone (NMP) and argon.

In addition to the model of Degen et al.,[2] an NMP solvent recovery system with a capacity of 4.1 million kg$_{NMP}$ year^{-1}, machine power of 2171.6 kW and heating power of 630 kW was added, based on the analysis of Ahmed et al.[206] Furthermore, to enable a scenario analysis of NMP-based vs. water-based cathode processing, the solid content in the mixing process and the natural gas power of the cathode dryer were adapted. Specific solid contents for each CAM were modeled ranging from 60 to 80% (Table S3, ESI†), based on data from Fraunhofer FFB, with a 10% lower solid content assumed for the aqueously processed electrodes.[207,208] Moreover, in the NMP scenario, the gas power input for drying was decreased by 41.8% to 480 kW compared to 825 kW in the model by Degen et al. due to additional heat input from the air-to-air heat exchanger of the solvent recovery system. A linear dependency from the system described by Ahmed et al. was assumed. For the aqueous scenario, an increase of 26.6% to 1045 kW was modeled, based on the work of Wood et al.[209]

3.3 LCA model

The calculated energy density, the BOM of the cell as well as the energy consumption and the BOM of cell production served as input for an LCA model. Seven commercially relevant SIB cell chemistries (P2/O3 NMMT, O3-ZNMT, O3-NFM111, NVPF, NFPP, Fe-PBA, and Mn-PBA, all vs. HC), including all three CAM classes, were modeled and compared with an LFP/graphite cell as a benchmark. The functional unit of the analysis was 1 kWh of produced battery cell energy. Fig. 2 shows the system boundaries and structure for this study. To reduce complexity and enhance comparability with other studies, only the CF was considered. The cradle-to-gate CF was determined by calculating GWP100 applying the method IPCC 2021 and economic allocation. Ecoinvent 3.9.1 was used as the LCI database.

For the active materials, new, industrial-scale synthesis models have been developed. The Na layered oxide CAMs were modeled by first regarding the precursor synthesis via co-precipitation, followed by a high-temperature calcination step, analogous to the production of Li-NMC and the approach presented by Dai et al.[210] The laboratory synthesis is mostly a simple solid-state synthesis, which was assumed in previous LCAs. However, the coinciding perception in the literature is that co-precipitation synthesis is most suitable for large-scale production, while solid-state synthesis is not scalable.[211–214] Moreover, specific changes compared to Li-NMC synthesis were included. For instance, in the co-precipitation process for Fe-containing layered oxides, such as O3-NFM, the chelating agent NH$_4$OH was replaced by oxalic acid because the ferrous amine complex is unstable and prone to decomposition.[214] In contrast to layered oxides, for polyanionic-type materials, solid-state synthesis, often with a preceding spray drying process, is the best applicable method for high yields at a large-scale.[94,212] The LFP synthesis by spray drying and sintering was modeled based on LCI data published by Quan et al.[215] The synthesis of polyanionic NVPF, applied in the Gen1 cells from Tiamat, was modeled based on the described solid-state reaction in the company's patent.[216] Large-scale synthesis of NFPP is typically conducted via spray drying, followed by a calcination step, analogous to LFP, based on industrial patents[90,102,103] and academic research.[217] The energy demand for the synthesis of the precursor VPO$_4$ and the CAMs NVPF and NFPP was assumed

This journal is © The Royal Society of Chemistry 2025

Energy Environ. Sci., 2025, **18**, 8104–8129 | 8113

to be equivalent to those for $FePO_4$ and LFP, given the high similarity of the synthesis processes. For PBAs, a solvent based precipitation synthesis was modeled, based on data from Wickerts et al.,[177] which originate from primary data of a PBA CAM manufacturer. The detailed description for each CAM synthesis, the underlying modeling parameters and the resulting LCI data are provided in Section S3.1.2 of the ESI.†

For the AAM, a new modeling approach was performed, equally for synthetic graphite (SGr) and HC, to enable a comparison that, for the first time, comprehensively includes gas and condensable volatiles for energy generation. For SGr production from green coke the two main energy intensive steps calcination and graphitization were considered. The calcination proceeds in a rotary kiln, and its material and energy flow calculation was based on a recent model by Li et al.[218] The energy produced by the combustion of volatiles was calculated from their lower heating values. The literature agrees that $\sim 35\%$ of the volatile matter is directly burned in the rotary kiln,[218–220] while the remaining $\sim 65\%$ is recovered and combusted in a downstream incinerator.[218,221] The heat generated in the incinerator was considered a co-product and allocated a share of the total CF using economic allocation. Table S4 (ESI†) lists the regarded material and energy streams during calcination. The graphitization process was modeled based on a recent study by Carrère et al.[222] that, for the first time, provided primary industrial synthesis data for battery-grade SGr production. While calcination was not modeled, their study includes additional milling, micronizing, coating and packaging steps, which were excluded in our analysis. The authors argue that additional treatments like particle size tailoring or coatings would be required for HC and the CAMs as well. However, due to a lack of data, these cannot be modeled and consequently were omitted for graphite production as well to maintain comparability. The production of natural graphite was modeled based on the LCI data from a Chinese manufacturer, published by Engels et al.[223] The coating step was not included, based on the argument made above.

For HC, the synthesis from commercially relevant precursors was regarded. Based on the conducted market review (Table 2) and the work of Liu et al.,[108] pitch (from petroleum or coal tar), lignin, coconut shells and phenolic resin precursors were attributed the highest relevancy. Pitch is used as the standard precursor for HC synthesis in this study, due to its position as the most widely produced precursor globally. Since no industrial data specifically for HC production were available, the calcination process applied in SGr production was taken as a reference, due to its high similarity. Pyrolysis of (biomass) precursors is often conducted in rotary kilns as well and proceeds at similar temperatures and durations.[224] Hence, for HC synthesis, the same energy demand (4.16 MJ $kg^{-1}_{precursor}$) as for green coke calcination was assumed. Biogenic carbon is treated as neutral (GWP = 0). Additionally, a scenario analysis (Fig. S3, ESI†) accounted for carbon sequestration during photosynthesis in the biomass precursors lignin and coconut shells. For the carbonization of pitch[225–228] and phenolic resin,[229,230] sufficient analytical analyses were found in the

literature to determine the amount and molecular composition of emerging volatile matter, which were applied in the model. The biomass precursors were modeled based on their relative composition of cellulose, hemicellulose and lignin (see the ESI†). The carbonization behavior of these three polymers, including the resulting side products (gases and bio-oil), was comprehensively researched in the literature, in contrast to the carbonization of many biomass HC precursors.[231,232] This approach has been validated experimentally by Stefanidis et al.,[232] showing only slight deviations due to limited heat and mass transfer in the experiment. The method has the additional advantage that it is easily transferable to a wide variety of biomass precursors, enabling a fast but also very comprehensive analysis. An in-depth description of the graphite and HC synthesis and the modeling approach is provided in Section 3.1 of the ESI,† listing all model parameters, including mass flows (with volatiles), energy flows and complete LCI data.

Material synthesis is assumed to be in China, while the modeled gigafactory is in Germany. Hence, as LCI input, natural gas and the electricity grid mix for China/Germany were used with the characterization factors of 0.0785/0.0552 kg CO_2-eq. MJ^{-1} and 0.954/0.471 kg CO_2-eq. kWh^{-1}, respectively, taken from ecoinvent 3.9.1. The complete LCI data for all materials and production steps analyzed in this study are provided in the ESI.†

4. Results and discussion

4.1 Energy density analysis

One of the key parameters that will decide on the degree of competitiveness and market penetration of SIBs is their energy density. Specific energy and energy density (Fig. 3) were calculated for pouch and prismatic cells, to highlight the significant impact of the cell format on the energy content, which is rarely acknowledged. Pouch cells show an increase in specific energy and energy density compared to prismatic cells of $\sim 25\%$ and $\sim 18\%$, respectively. The reasons are rooted in the architecture of the prismatic cell housing, with a higher mass and more dead volume, which increases the electrolyte demand. Consequently, for the pouch cell, an electrolyte amount equal to 1.3 times the pore volume of electrodes and separator was applied in the model, and for the prismatic cell, this ratio was set to 1.8, hence increasing the cell weight. Moreover, due to the larger prismatic housing, the cell is divided into two separate cell stacks, which ensures safety but decreases energy density.

The modeled cells contain the commercially relevant CAMs listed in Table 1 and HC as AAM, and the cathode thickness was set to 90 μm. For simplification, the cells are in the following only addressed with the name of the CAM. In the HC-basic (325 mAh g^{-1}, 0.3 V vs. Na/Na$^+$, 1.5 g cm^{-3}) scenario the LFP cell is clearly superior, especially regarding energy density (Fig. 3a and c). While the pouch LFP cell has a specific energy/energy density of 214 Wh kg^{-1}/507 Wh L^{-1}, the layered oxide-based SIB cells are in the range of 147–206 Wh kg^{-1}/333–419 Wh L^{-1}, the polyanionic cells reach 158–192 Wh kg^{-1}/310–366 Wh L^{-1}

8114 | Energy Environ. Sci., 2025, 18, 8104–8129

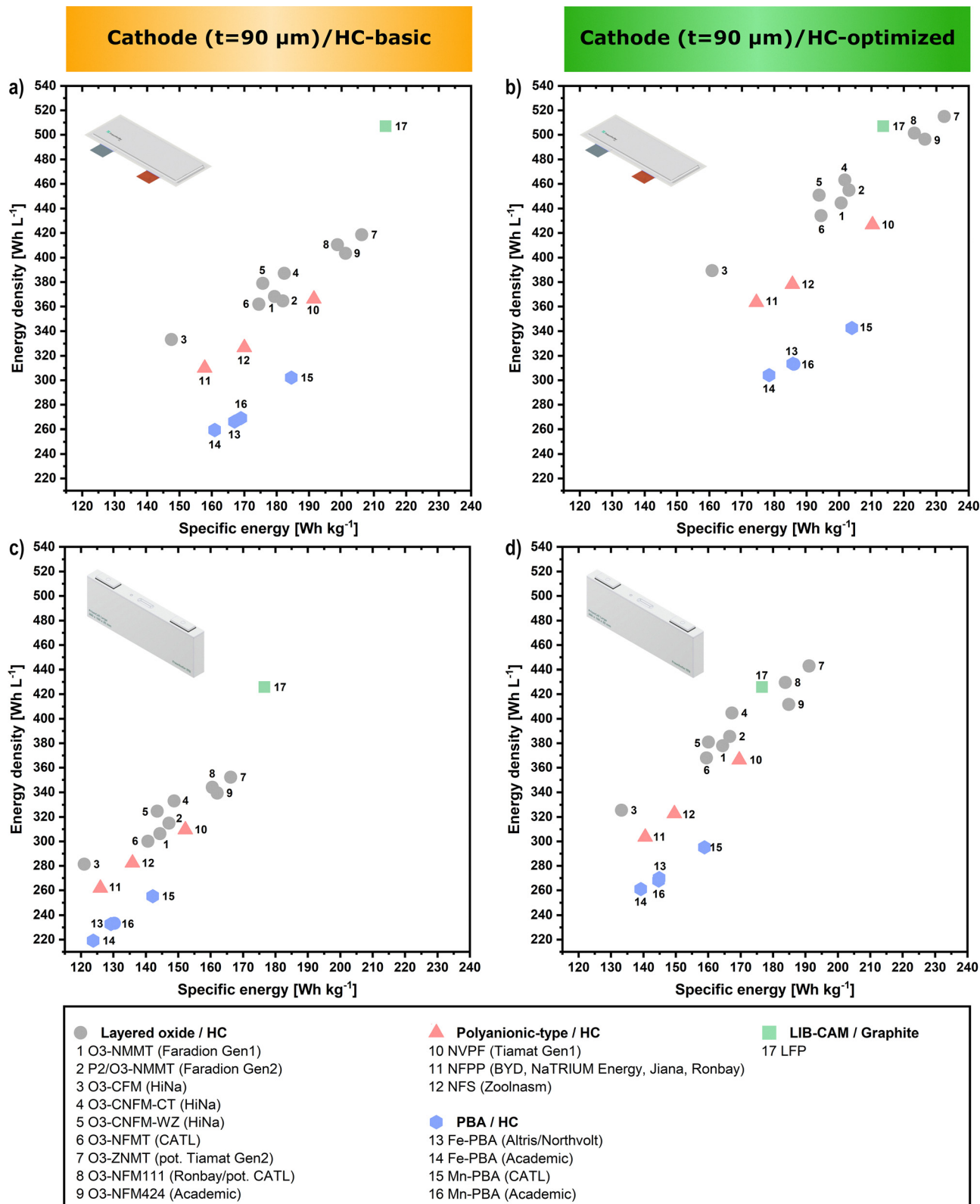This journal is © The Royal Society of Chemistry 2025

Fig. 3 Specific energy and energy density of commercially pursued SIB cell chemistries, distinguishing between pouch (a) and (b) and prismatic (c) and (d) cell format and HC-basic (a) and (c) and HC-optimized (b) and (d) as the AAM. The cell metrics are 300 mm × 100 mm × 30 mm for the prismatic cell and 317 mm × 134 mm × 13 mm for the pouch cell. The cathode coating thickness is set to 90 μm for all cells. HC-basic: 325 mAh g^{-1}, 0.3 V $vs.$ Na/Na$^+$, 1.5 g cm^{-3}, and HC-optimized: 375 mAh g^{-1}, 0.2 V $vs.$ Na/Na$^+$, 1.8 g cm^{-3}.

and the PBA cells achieve 161–185 Wh kg^{-1}/260–302 Wh L^{-1}. Although several SIB-CAMs, especially Ni-rich layered oxides, match or surpass LFP in specific energy and energy density (Fig. 1), the lower cell-level performance of SIBs is primarily due to the inferior capacity, voltage and density of HC relative to graphite. The specific energy and energy density of prismatic cells is systematically lower, but the observed trends remain consistent. Slight deviations in the trends can be ascribed to the increased number of stacks in the prismatic cell, as elaborated below.

In the HC-optimized (375 mAh g^{-1}, 0.2 V $vs.$ Na/Na$^+$, 1.8 g cm^{-3}) scenario (Fig. 3b and d), SIB cell chemistries from all material classes reach competitive, specific energies or even surpass LFP: O3-NFM111/424 (+5%/+6% for pouch), O3-ZNMT (+9%), NVPF (−1%), and Mn-PBA (−5%). The named layered oxide cells are the only chemistries which reach competitive volumetric energy densities to LFP, O3-ZNMT being the modeled cell that delivers the highest energy density (515 Wh L^{-1} for pouch). The majority of the layered oxide-based SIBs still show a 10–15% lower energy density than LFP/graphite, polyanionic-type cells −16% to −28% and PBA cells −32% to −40% decreased values.

The results highlight the need to increase the anode performance by optimizing HC or, alternatively, develop next-generation AAMs with higher capacities, $e.g.$ by adding P or alloying materials like Sn, to achieve competitiveness with LFP-based LIBs. Furthermore, the results must be critically examined since the energy density is not the only parameter which must be maximized for commercial application. Especially, high cycling stability is crucial. Particularly, several layered oxide cells, among them also O3-ZNMT, must still be optimized towards a higher cycle life, which, among others, might demand lower cut-off voltages, hence reducing specific energy/energy density. Nevertheless, Na layered oxide-based cells offer the highest energy densities among SIBs, demonstrating the highest potential to compete with LIBs in mobile applications such as EVs. Cells based on polyanionic compounds exhibit a good cycle life, even at high rates.[33,233,234] This makes them promising for high-power but also ESS applications, given their competitive specific energy. Of course, additional factors, among others sustainability (see Section 4.2) and cost must be acknowledged as well. ESS applications also seem to be the best fit for PBA-based cells due to their low energy density but competitive specific energy.

Next to the choice of cell chemistry, the electrode thickness must be tailored depending on the application. On the one hand, high electrode thickness increases electrode loading and, thereby, the energy density of the cell. On the other hand, thicker coatings limit the rate capability, which results in compromises. The increase in energy density with higher thickness/loading has already been shown in previous work.[38,235–237] However, to the authors knowledge, it has not been considered that the energy content in practical cells does not rise steadily with electrode thickness due to the limited and fixed size of the cell housing, as shown in Fig. 4. Here, the specific energy and energy density of selected cell chemistries in the prismatic, HC-basic scenario are illustrated as a function of the cathode
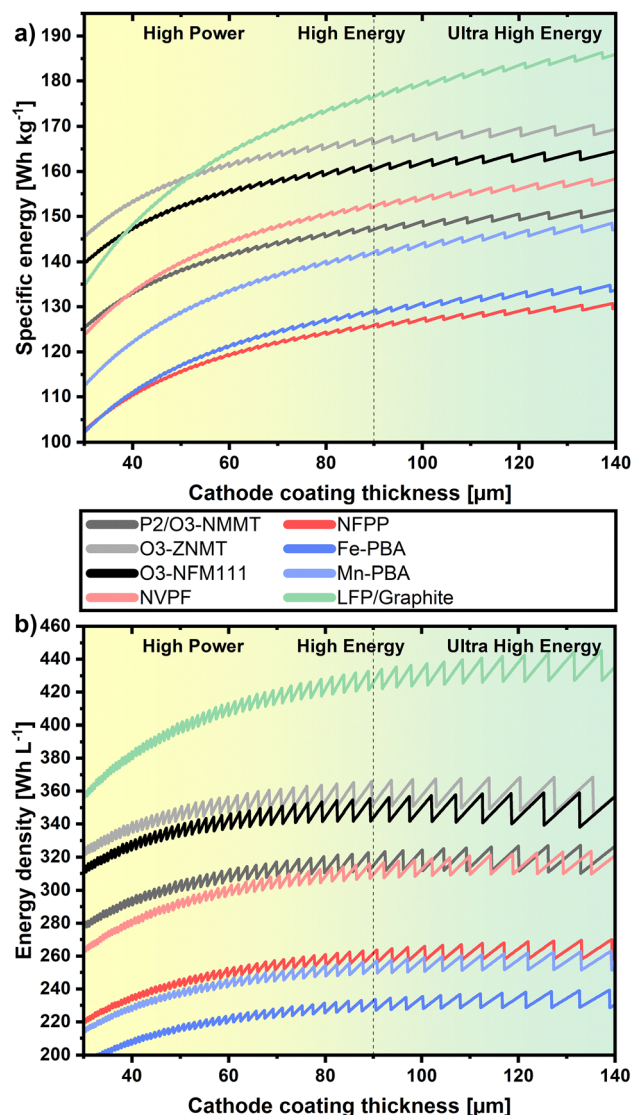

Fig. 4 Specific energy (a) and energy density (b) for selected SIB cell chemistries in the prismatic cell, HC-basic scenario depending on the cathode coating thickness, compared to an LFP/graphite cell. For Fe-PBA and Mn-PBA the electrochemical data from Altris/Northvolt and CATL are applied (cell 13 and 15 from Fig. 3). In this study the coating thickness was set to 90 μm, which is marked for clarification.

coating thickness. The energy metrics show a limited growth curve regularly interrupted by sharp decreases that originate from the reduction of electrode layers that fit into the cell housing with increasing electrode thickness. The decreases are especially significant in terms of volumetric energy density (up to −23 Wh L^{-1} for O3-ZNMT) since, in contrast to weight and capacity, the cell volume always remains constant. This fact must be considered in cell and electrode design to maximize the cell's energy content and reduce costs per kWh. Furthermore, cells based on high-density CAMs show a comparatively high energy content at low coating thickness. However, their specific energy and energy density plateau faster and show larger drops. Moreover, with rising coating thickness the influence of cell voltage increases. This is exemplified by the narrowing gap in

8116 | Energy Environ. Sci., 2025, 18, 8104–8129

This journal is © The Royal Society of Chemistry 2025

Table 3 BOM and nominal energy of modeled prismatic cells in the HC-basic scenario. CMC = carboxymethyl cellulose, SBR = styrene–butadiene rubber, and PVDF = polyvinylidene fluoride

Component	P2/O3-NMMT Mass [g]	O3-ZNMT Mass [g]	O3-NFM111 Mass [g]	NVPF Mass [g]	NFPP Mass [g]	Fe-PBA Mass [g]	Mn-PBA Mass [g]	LFP/graphite Mass [g]
Anode								
AAM	347.5	394.8	386.3	290.4	300.8	267.4	265.7	387.6
CMC	7.2	8.2	8.0	6.1	6.3	5.6	5.5	8.1
SBR	5.5	6.2	6.1	4.6	4.7	4.2	4.2	6.1
Carbon black	1.8	2.1	2.0	1.5	1.6	1.4	1.4	2.0
Al/Cu-CC	38.3	32.9	34.2	46.6	46.6	46.6	46.6	164.9
Cathode								
CAM	672.5	615.8	641.1	612.9	634.7	451.5	448.7	726.0
PVDF	14.0	12.8	13.4	12.8	13.2	9.4	9.3	15.1
Carbon black	14.0	12.8	13.4	12.8	13.2	9.4	9.3	15.1
Al-CC	34.8	29.7	31.0	42.6	42.6	42.6	42.6	45.2
Other								
Electrolyte	424.5	430.5	431.3	425.2	432.4	409.2	408.1	423.6
Separator	36.6	31.3	32.6	44.4	44.4	44.4	44.4	47.0
Cell housing	330.0	330.0	330.0	330.0	330.0	330.0	330.0	330.0
Total cell mass	1926.7	1907.1	1929.4	1829.7	1870.4	1621.7	1615.7	2170.8
Nominal energy [Wh cell^{-1}]	283.5	317.0	309.6	278.5	235.6	209.5	229.7	383.4
Specific energy [Wh kg^{-1}]	147.1	166.2	160.5	152.2	126.0	129.2	142.2	176.6
Energy density [Wh L^{-1}]	315.0	352.2	344.0	309.5	261.8	232.8	255.2	426.0

specific energy between the higher voltage Mn-PBA cell and the P2/O3-NMMT cell as the cathode thickness increases. For the volumetric energy density, the effect is smaller because it scales with the material density as well. Notably, at lower electrode thicknesses, SIBs are more competitive with LFP/graphite in terms of specific energy because the Al current collector (CC) has a lower density compared to the Cu CC applied in LIBs.[38]

4.2 Carbon footprint analysis

The basis for the LCI is the BOM of the modeled cells, an output of the battery cell model, which is shown in Table 3 for prismatic cells in the HC-basic scenario. The cradle-to-gate CF is quantified as the cumulative impact from the individual cell components, the materials used in cell production, and the energy consumed throughout cell production. Two parameter variations were analyzed: the impact of applying HC-optimized resulting in higher energy density and the impact of aqueous cathode processing.

4.2.1 Cradle-to-gate CF of SIB cells vs. LFP/graphite. The results for prismatic cells in the HC-basic and HC-optimized scenarios are presented in Fig. 5. The CF of the LFP/graphite benchmark is highly dependent on the choice of SGr or natural graphite (NGr) as the AAM. The LFP/SGr cell exhibits a CF of 76.1 kg CO_2-eq. kWh^{-1}, which is 35% higher compared to the NGr-based LFP cell (56.5 kg CO_2-eq. kWh^{-1}). Current market shares of SGr and NGr in LIBs are approximately 75% and 25%, respectively, with a further increase in SGr application anticipated.[222,238,239] To ensure a meaningful comparison and account for the fact that LIB anodes increasingly contain blends of SGr and NGr,[240] LFP/graphite with an AAM consisting of 75 wt% SGr and 25 wt% NGr was selected as the primary benchmark. The resulting CF of 71.2 kg CO_2-eq. kWh^{-1} is illustrated as a horizontal reference line in Fig. 5.

Generally, in the HC-basic scenario, the CFs of all analyzed SIB and LIB cell chemistries are within the same order of magnitude and mostly show CF differences <20%. All SIB cells show higher CFs, compared to the LFP/graphite benchmark. However, the best-performing SIB cell, O3-ZNMT (71.6 kg CO_2-eq. kWh^{-1}) nearly matches the benchmark ($\Delta < 1\%$). Most other SIB cell chemistries show slightly to moderately increased values, ranging from 3 to 17% above the reference. Only the NVPF cell (97.3 kg CO_2-eq. kWh^{-1}) and the LFP cell with 100% NGr (56.5 kg CO_2-eq. kWh^{-1}) deviate substantially from the benchmark, by +37% and −21%, respectively.

Faradion's P2/O3-NMMT cell chemistry exhibits a higher cradle-to-gate CF of 83.6 kg CO_2-eq. kWh^{-1} compared to the other layered oxide-based SIBs, mainly due to its lower energy density. The NFPP and Mn-PBA cells show very similar values to the LIB benchmark with 73.4 kg CO_2-eq. kWh^{-1} and 75.8 kg CO_2-eq. kWh^{-1}, respectively.

In the HC-optimized scenario, the increase in energy density results in a CF reduction of 7–11%. Consequently, four out of the seven evaluated SIB cells exhibit a lower CF than the benchmark, while only NVPF shows a higher impact than LFP with 100% SGr. This result underlines the importance of increasing energy density, not only for competitiveness regarding electrochemical performance but also for environmental footprint.

Comparing the results with Peters et al.,[30] so far the most comprehensive LCA study on SIBs, the obtained cradle-to-gate CFs are higher for NMMT (+65%) and LFP/graphite (+43%), while Fe-PBA has a lower CF (−6%). Generally, the CFs of the different cell chemistries show smaller deviations compared to Peters et al.'s results and LFP's CF is increased relative to the SIBs. Looking at the emission breakdown, significant differences to Peters et al. regarding the impacts of cell housing, the
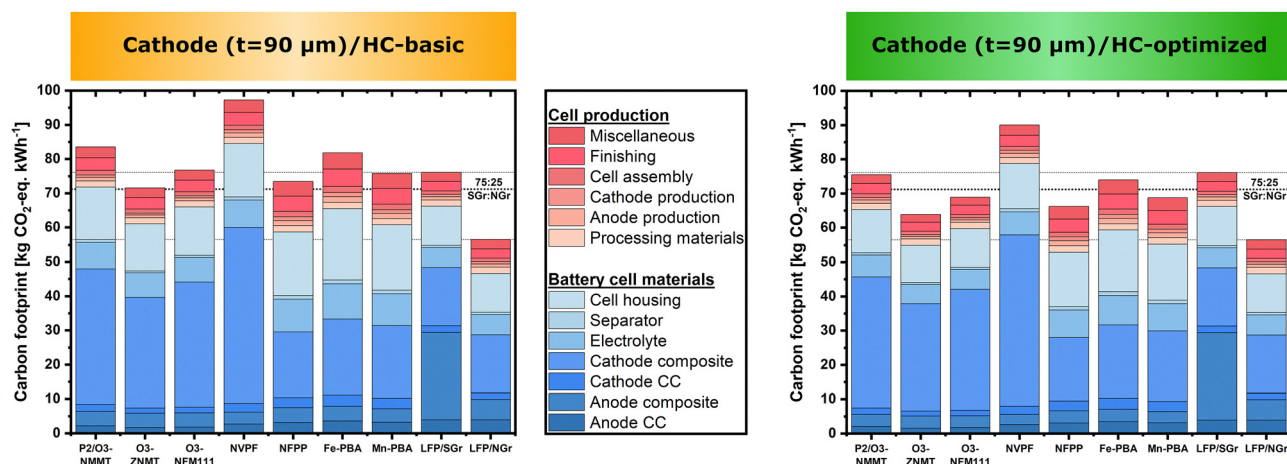
This journal is © The Royal Society of Chemistry 2025

Energy Environ. Sci., 2025, 18, 8104–8129 | 8117

Fig. 5 CF of selected SIB cell chemistries in comparison with LFP/graphite in prismatic cell format in the HC-basic (left) and HC-optimized (right) scenarios. The underlying cell is the same as in Fig. 3c and d with a cathode thickness of 90 μm. For Fe-PBA and Mn-PBA the electrochemical data from Altris/Northvolt and CATL are applied. The category "miscellaneous" contains the material handling operations during cell production, the dry rooms (dew point: −40 °C) and the NMP recovery system. Processing materials contain solvents for mixing, compressed air, argon and nitrogen. The horizontal line labeled "75 : 25 SGr : NGr" illustrates the CF of an LFP cell containing a graphite blend composed of 75 wt% SGr and 25 wt% NGr. The ratio equals the current market shares of SGr and NGr, thus is used as the benchmark.

active materials, and cell production are observable. These are also the largest sources of GHG emissions and, therefore, examined in detail in the following.

Regarding the cell housing, the difference to Peters *et al.* is rooted in the different amount of Al casing. This work models a large, commercial, prismatic cell housing, with the majority of the 330 g cell housing weight stemming from Al, a high-impact material (13.8 kg CO_2-eq. kg^{-1}). Peters *et al.* model a much lighter housing (34–61 g depending on cell chemistry), indicating a pouch cell format, which consequently requires less Al, resulting in fewer GHG emissions.

For all SIB cell chemistries, the cathode composite is the cell component that causes the most GHG emissions (19.1–51.4 kg CO_2-eq. kWh^{-1}). In the case of LFP/graphite, the cathode also accounts for a substantial CF (17.0 kg CO_2-eq. kWh^{-1}); however, it is exceeded by the emissions associated with the anode composite (blend: 20.6 kg CO_2-eq. kWh^{-1}, SGr: 25.5 kg CO_2-eq. kWh^{-1}, NGr: 5.9 kg CO_2-eq. kWh^{-1}). This represents a large deviation from SIBs, where the HC-based anode only allocates ∼4 kg CO_2-eq. kWh^{-1}.

4.2.2 CF of SIB and LIB active materials. In light of the high share of the active materials to the total CF, Fig. 6 illustrates a comparison of the material-specific impacts of the modeled active materials [kg CO_2-eq. kg^{-1}]. Furthermore, the three main sources of GHGs associated with their synthesis are depicted, respectively. On the one hand, the CFs of all SIB-CAMs besides NFPP (5.8 kg CO_2-eq. kg^{-1}) are considerably higher compared to LFP (7.6 kg CO_2-eq. kg^{-1}), ranging from 9.0 kg CO_2-eq. kg^{-1} for Fe-PBA to 22.0 kg CO_2-eq. kg^{-1} for NVPF.

On the other hand, the CF of pitch-based HC AAM (3.2 kg CO_2-eq. kg^{-1}) is nearly a magnitude lower compared to SGr (25.1 kg CO_2-eq. kg^{-1}). The difference to NGr (5.7 kg CO_2-eq. kg^{-1}) is considerably smaller. Biomass-derived HCs from coconut shells and lignin exhibit comparable CFs of

2.6 kg CO_2-eq. kg^{-1} and 3.4 kg CO_2-eq. kg^{-1}, respectively. However, when biogenic carbon uptake during biomass growth is accounted for, the CF is significantly reduced to 0.3 kg CO_2-eq. kg^{-1} and 0.7 kg CO_2-eq. kg^{-1} (Fig. S3, ESI†). The high CF of SGr mainly roots from the energy-intensive graphitization process, where needle coke powder is graphitized in graphite crucibles for several weeks at ∼3000 °C, requiring 16 kWh kg^{-1} electricity, as recently disclosed by Carrère *et al.*[222] Additionally, about 30% of SGr's footprint stems from the graphite crucibles, which are consumed during graphitization. In contrast, HC is produced *via* carbonization at distinctively lower temperatures (900–1600 °C). The process only lasts several hours, thus requiring substantially less carbonization energy. Moreover, unlike biomass-based and NGr precursors, which contain high levels of ash and inorganic impurities, pitch-based HC synthesis does not require acid purification. A detailed description of the acid treatment and its associated environmental impacts is provided in the ESI.† Additional pre- and post-treatment steps, as well as a pre-oxidation/carbonization, might be added (Fig. S2, ESI†). However, compared to the carbonization process, pre- and post-treatments have a small or even negligible energy demand.[179] Based on this fact and the conjuncture that no industrial data for HC production are available, only the energy-intensive synthesis steps for HC and SGr, but also CAM production are regarded. Carrère *et al.* even calculate a CF of 42 kg CO_2-eq. kg^{-1} for SGr, and the additional footprint is caused by milling, micronizing, coating and packaging steps. Based on the argument made above (see Section 3.3), these steps were disregarded in this study. The same applies for the coating of NGr. The coating step significantly increases the CF to 9.6 kg CO_2-eq. kg^{-1}, as shown by Engels *et al.*,[223] who provided primary data from a Chinese NGr producer. While this approach ensures comparability, it underestimates the total CF of the active materials and, ultimately, the battery cells. This
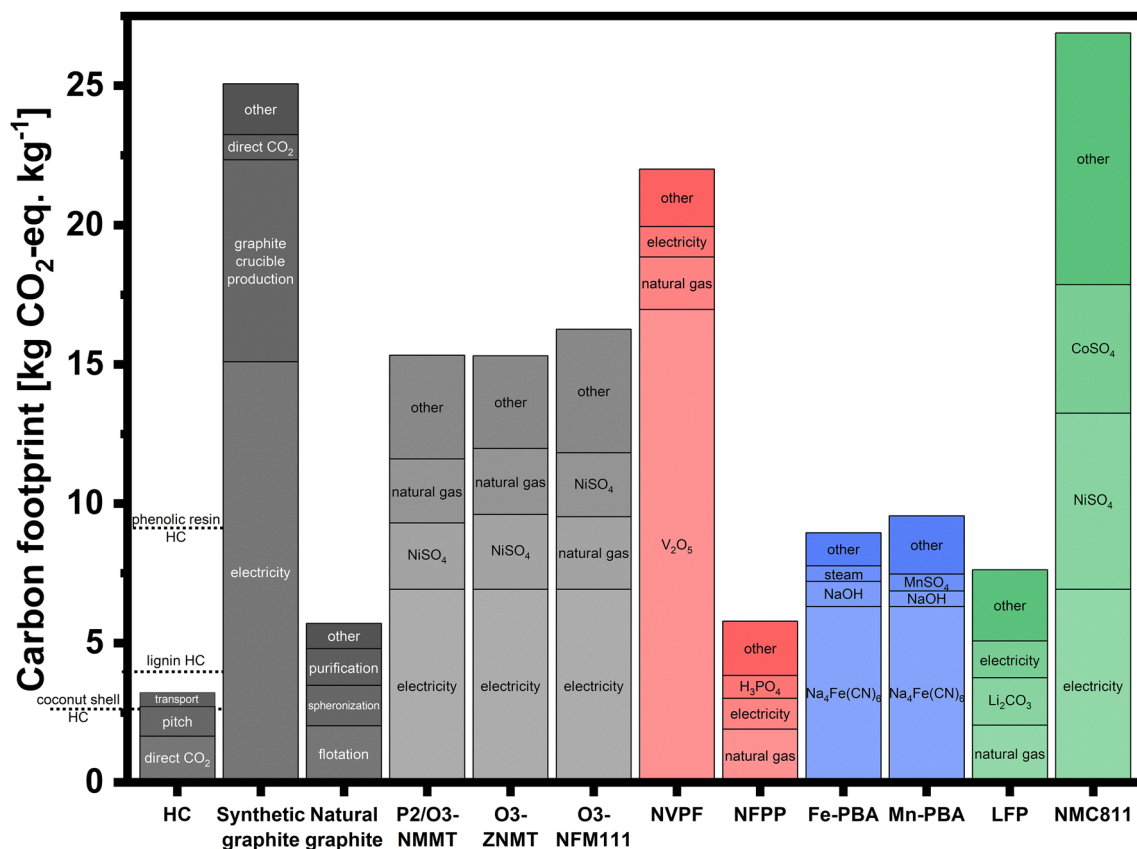
8118 | *Energy Environ. Sci.*, 2025, **18**, 8104–8129

This journal is © The Royal Society of Chemistry 2025

Fig. 6 Comparison of the mass related CFs of SOTA active materials for SIBs and LIBs. The three primary GHG emission sources associated with their synthesis are also illustrated.

highlights the critical need for comprehensive, industrial primary data for AAM and CAM synthesis to improve the accuracy of LCAs for battery systems. The studies of Carrère *et al.* and Engels *et al.* represent important steps towards this goal. Carrère *et al.*, for the first time, holistically quantified the CF of battery-grade SGr based on industrial primary data. Previous LCAs of LIBs generally applied graphite LCI data from ecoinvent (based on Dunn *et al.*[241]), Surovtseva *et al.*[242] or the GREET model.[243] However, in all cases, the less energy-intensive Acheson block process route, applied in primary aluminum production, is modeled, which largely varies from the Acheson powder process used to yield battery-grade SGr.[222] This resulted in a significant under-estimation of the CF of SGr, and, therefore of LIBs.

Moreover, a new modeling approach, for the calcination process to produce needle coke, which is not included in the work of Carrère *et al.*, is presented that, for the first time, comprehensively includes gas and condensable volatiles for energy generation (see the ESI†). The calcination of green coke is conducted in rotary kilns at ~1400 °C, powered by natural gas and volatile combustion. About 35% of the volatile matter is burned directly in the rotary kiln.[218–220] The remaining 65% of volatile matter is recovered and combusted in a downstream incinerator.[218,221] Carbonization of (biomass) precursors to pro-duce HC is often carried out in rotary kilns as well and proceeds at similar temperatures and durations.[224] In the absence of industrial data specific to HC production, the calcination process

was used as a reference. In the case of HC produced from pitch, the precursor with the highest large-scale production potential,[108] the volatiles combusted in the carbonization unit produce more energy (8.65 MJ kg$^{-1}_{\text{pitch-HC}}$) than required for the carbonization (6.40 MJ kg$^{-1}_{\text{pitch-HC}}$). This makes the process self-sustaining, which agrees with previous assumptions in the literature, now quantified by applying the lower heating values of the respective volatile matter (ESI,† Section S3.1.1).[177] The same is true for the biomass precursors coconut shells and lignin. Due to their lower carbon yield, the required energy is rising (*e.g.* 15.0 MJ kg$^{-1}_{\text{coconut-HC}}$), but the same applies to the volatile combustion energy during pyrolysis (15.1 MJ kg$^{-1}_{\text{coconut-HC}}$). Only for phenolic resin, additional natural gas must be supplied to fuel the carbonization, comparable to green coke calcination. In the absence of industrial primary data, this approach still includes a degree of uncertainty. Nevertheless, the authors want to emphasize the significance of volatile matter combustion to the energy balance of HC and needle coke production. This energy contribution was neglected or highly simplified in past studies. Especially, the differing molecular composition of the volatile matter, depending on the respective precursor, has not been quantitatively considered before.

The excess heat generated is treated as a co-product, with its share of the total CF is determined through economic alloca-tion. This results in a CF reduction for HC of 1–5%, depending on the precursor. When biogenic carbon is accounted for,

This journal is © The Royal Society of Chemistry 2025

Energy Environ. Sci., 2025, **18**, 8104–8129 | 8119

biomass-derived HC becomes nearly burden-free (e.g. 0.3 kg CO_2-eq. $kg^1_{coconut-HC}$). However, the low GHG emissions attributed to pitch and biomass precursors must be put into perspective since they are by- or waste-products with low or no allocated economic value, leading to low CFs. This could significantly increase in the case of a sharp ramp-up of HC production and increasing demand for the respective precursors. The detailed CF allocation of all assessed HCs is illustrated in Fig. S3 (ESI†).

Looking at the CF of the CAMs, no advantage for SIB materials can be observed. In contrast, LFP exhibits a comparably low CF with 7.6 kg CO_2-eq. kg^{-1}, while NMC811 shows the highest CF of all observed active materials (26.9 kg CO_2-eq. kg^{-1}). For Na and Li layered oxide CAMs, the synthesis energy, especially the electricity for the calcination, is the largest CF contributor. This originates from the high energy demand (7.26 kWh kg_{CAM}^{-1}) in combination with the carbon intensive Chinese electricity mix (0.95 kg CO_2-eq. kWh^{-1}). With 6.9 kg CO_2-eq. kg^{-1}, the electricity makes up nearly half of the footprint of Na layered oxides. Additionally, the high impact of $NiSO_4$ (5.0 kg CO_2-eq. kg^{-1}) is driving the CF of the layered oxides. Nevertheless, compared to NMC811, the Na layered oxides have a significantly reduced CF (all ∼15 kg CO_2-eq. kg^{-1}) due to their lower Ni content and the substitution of the high-impact precursors LiOH (5.0 kg CO_2-eq. kg^{-1}) and $CoSO_4$ (28.9 kg CO_2-eq. kg^{-1}) with low impact materials like NaOH (1.3 kg CO_2-eq. kg^{-1}) and $FeSO_4$ (0.3 kg CO_2-eq. kg^{-1}).

Among the seven SIB-CAMs assessed, NFPP has the lowest mass-based CF, at 5.8 kg CO_2-eq. kg^{-1}, making it the only SIB-CAM with a lower impact than LFP. NFPP and LFP are synthesized via nearly identical process routes, involving spray drying followed by calcination. Accordingly, the same energy demand was assumed for their synthesis. The primary reason for the reduced CF is the substitution of high-impact Li_2CO_3 (7.7 kg CO_2-eq. kg^{-1}) with Na_2CO_3 (1.3 kg CO_2-eq. kg^{-1}).

Despite its equally low synthesis energy, NVPF shows the highest CF of all SIB CAMs, majorly attributed to the precursor V_2O_5. The high impact material (41.0 kg CO_2-eq. kg^{-1}) makes up 77% of the GHGs allocated to NVPF production. V_2O_5 is extracted from vanadium-bearing slag, a by-product of crude steel production.[244] By applying economic allocation, a substantial share of the GHG emissions linked to the energy-intensive crude steel production was allocated to vanadium slag and, ultimately, V_2O_5 due to the high price of the precursor. The result is a very high CF of V_2O_5 and, ultimately, NVPF. New LCI data for V_2O_5 are listed in the ESI,† based on industrial data from a large-scale production plant in China, the main producing country of V_2O_5.[245]

Prussian white CAMs are industrially synthesized by applying a low-temperature, solvent-based precipitation method with comparatively low energy demand (0.26 kWh kg^{-1}_{CAM}).[133,177,246] The low energy consumption of the synthesis results in reduced GHG emissions, classifying PBAs as a low-CF CAM class among SIBs. Nevertheless, due to the high consumption and impact of the sodium ferrocyanide ($Na_4Fe(CN)_6$) precursor (4.5 kg CO_2-eq. kg^{-1}), that makes up 70% of Fe-PBA's emissions, the total CF is still higher compared to LFP. The high CF of $Na_4Fe(CN)_6$ mainly originates from the precursor HCN (7.8 kg CO_2-eq. kg^{-1}) and its GHG intensive production from methane and ammonia.[247]

4.2.3 CF of gigafactory-scale cell production. In addition to the materials, cell production within the gigafactory is the second substantial source of GHG emissions, contributing to the cradle-to-gate CF. Cell production, namely the impact of processing materials like NMP and the manufacturing energy, makes up 13–20% of the cradle-to-gate CF, ranging between 10.5 kg CO_2-eq. kWh^{-1} (O3-ZNMT) and 16.3 kg CO_2-eq. kWh^{-1} (Fe-PBA) in the HC-basic scenario. For LFP-cells the production footprint is 9.8 kg CO_2-eq. kWh^{-1}. By applying HC-optimized, the CF is reduced to 8.9–14.6 kg CO_2-eq. kWh^{-1} due to the increase in energy density. It is important to note that, unlike the material synthesis, cell production is modeled for a location in Germany rather than China, utilizing an electricity mix with only half the carbon intensity. When Chinese grid emission factors are applied, the CF of cell production in the HC-basic scenario increases to 17.2–27.3 kg CO_2-eq kWh^{-1}. As a result, the relative contribution of cell manufacturing to the total CF rises significantly, reaching 20–30%, highlighting the influence of site selection on the CF.

The differing impacts between cell chemistries are mainly attributed to the variations in energy density. The lower energy density of SIBs proves disadvantageous, because it requires the production of more cells to reach the same total energy output. Consequently, the CF for cell production is higher for SIBs compared to LFP/graphite cells. The same principle applies to production costs.[248] Additionally, the applied solid content in the slurry affects the mixing throughput. The manufacturing energy consumption was calculated based on Degen et al.,[2] utilizing primary data from machine suppliers and modeled according to the production model outlined above. The resulting emissions are 2–3 times lower compared to Peters et al.[30] or Wickerts et al.[177] Given the high reliability of the data (±10% uncertainty),[2] the authors are confident in presenting realistic values, thereby supporting the argument made by Peters et al. that the footprint of cell manufacturing has been overestimated in previous studies.

A further breakdown of the CF into the single process steps is shown in Fig. 7. The formation process results in the largest CF contribution for all cell chemistries, followed by the dry rooms as well as coating and drying of the electrodes. One strategy to reduce the environmental impact of battery cell production is to avoid the toxic and costly solvent NMP, which requires a laborious solvent recovery system. While graphite- and HC-based anodes are being processed with water already, for cathode production, NMP is still SOTA. To quantify the advantage in terms of GHG reduction, Fig. 7 compares NMP-based cathode processing with the aqueous alternative. Although NMP has a high impact (6.7 kg CO_2-eq. kg^{-1}), its contribution to the CF of cell manufacturing is small (<0.1 kg CO_2 kWh^{-1}). This is a consequence of the high NMP recovery rate (∼98%), meaning that only about 2% of the NMP required for slurry mixing is supplied as virgin material. In contrast, the NMP solvent recovery system itself contributes up to 1 kg CO_2 kWh^{-1} or 6–9% of the emissions from cell manufacturing. Applying aqueous processing

8120 | Energy Environ. Sci., 2025, **18**, 8104–8129

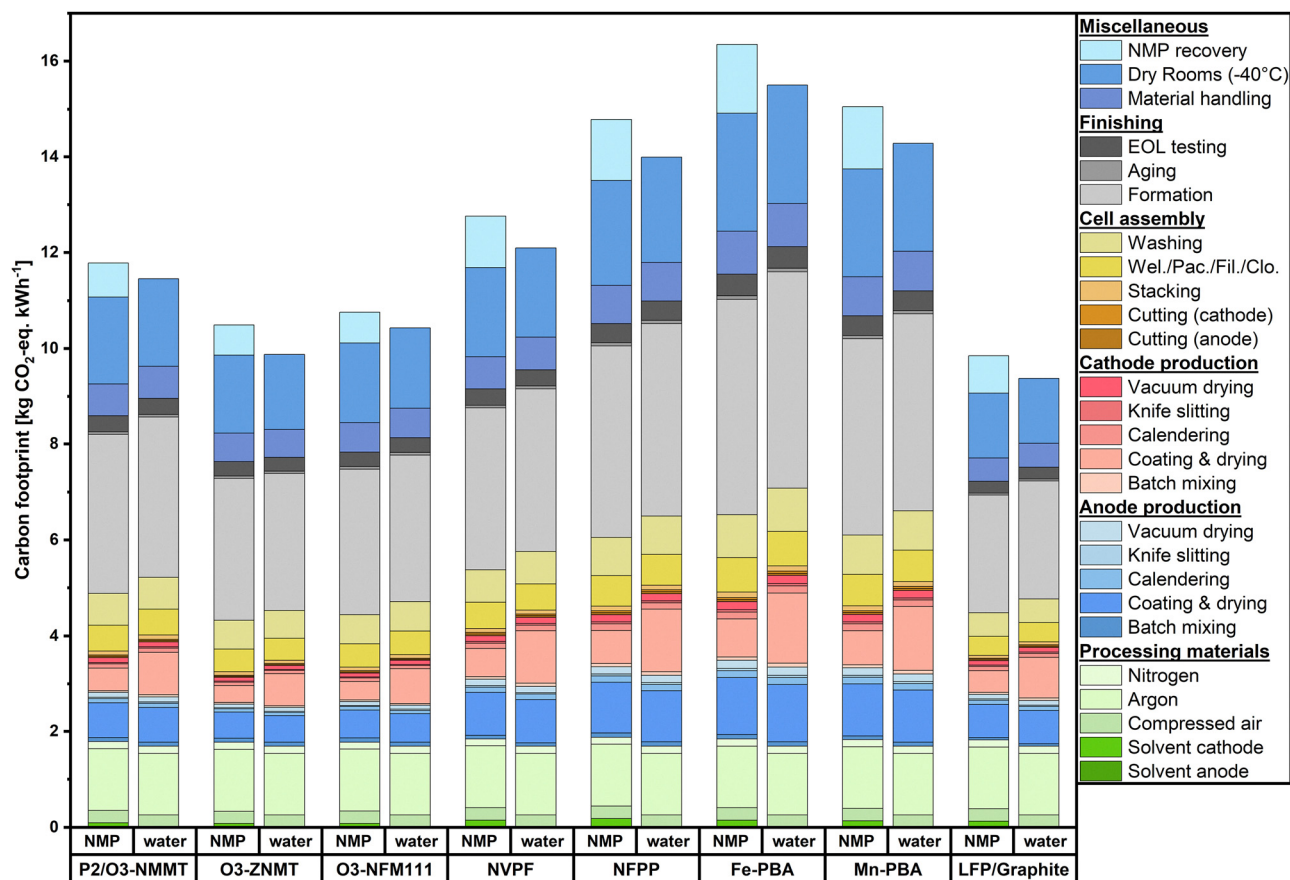This journal is © The Royal Society of Chemistry 2025

Fig. 7 CF of prismatic cell production for selected SIB cell chemistries in the HC-basic scenario compared to LFP/graphite cells, distinguishing between NMP-based and aqueous cathode processing. Wel. = welding, Pac. = packaging; Fil. = electrolyte filling, Clo. = closing, EOL = end of line.

results in an emission reduction of 3–5% for cell manufacturing. The fact that the total GHG reduction is smaller than the emissions saved by omitting the solvent recovery system is mainly based on the differing gas power input of the drying unit. In the NMP scenario, the air-to-air heat exchanger of the solvent recovery system feeds waste heat into the dryer, thereby reducing its natural gas demand compared to aqueous cathode production. This assumption is only valid if the solvent recovery system is integrated into the gigafactory and not outsourced. Furthermore, the reduced solid content for aqueous processing (Table S3, ESI†) lowers the throughput of the mixing process, hence increasing emissions.

The resulting CF reduction at the cell level of 3–5% is additionally increased by the material switch from high-impact PVDF (61.1 kg CO_2-eq. kg^{-1})[249] to less GHG intensive SBR (2.5 kg CO_2-eq. kg^{-1}) and CMC (4.8 kg CO_2-eq. kg^{-1}). Even though the CF reduction is small, it must be considered that a switch from NMP to aqueous processing has many other benefits beyond GHG reduction. The advantages entail improvements in the area of other environmental impact categories (e.g. human toxicity), cost reductions due to the abolishment of the NMP recovery system, reduced safety requirements and lower disposal costs.[209,250] On top of that, aqueous processing eases battery recycling, especially direct recycling.[251] Apart from that, the influence on electrode quality must be considered. In this work, no effect on the battery's energy density was assumed since,

despite known challenges and degradation effects, especially for layered oxide CAMs,[252–254] tremendous progress has been made. Recent studies show comparable or even enhanced performance for aqueously processed cathodes.[255–257] Nevertheless, a significant reduction in energy content, and thereby increased CO_2-eq. kWh^{-1}, will likely more than outweigh the presented reduction. Hence, regarding CF, a switch to aqueous processing is only advisable if the electrochemical performance is at least comparable to the NMP-based process. If NMP is applied, the recovery system should be optimized for high recovery rates, energy efficiency and installed onsite to minimize the environmental footprint.

5. Conclusions

SIBs are entering the battery market with several companies pursuing plans for gigafactory-scale production. The "drop-in" capability on existing LIB manufacturing lines substantially reduces market entry barriers and accelerates production scale-up. SIBs are particularly developed for cost-sensitive markets and applications, such as ESS and EVs. Consequently, LFP-based LIBs are the main competing technology. Beyond costs, SIBs must challenge LIBs in terms of electrochemical performance and sustainability, which was analyzed in this work.

The aim of this study was to quantitatively benchmark the energy density and CF of SOTA and promising SIB cell chemistries in comparison to LFP/graphite, assessing the current development stage and competitiveness of SIBs. Based on a screening of commercially pursued SIB active materials and their electrochemical properties, a comprehensive modeling approach was applied to determine the energy density and CF of SIB cells produced at gigafactory-scale. The performed LCA covers the whole value chain, from raw material extraction and active material synthesis to gigafactory-level production, in all cases applying industry-scale data. Moreover, this analysis identifies key factors for improving SIBs on the GWh year^{-1} production scale to further increase their industrial relevance.

HC is currently the only commercially relevant AAM for SIBs, whereas leading SIB cell manufacturers are pursuing CAM representatives from all main material classes, namely layered oxides, polyanionic compounds, and PBAs. In a HC-basic scenario, SIB cells composed of SOTA HC (325 mAh g^{-1}, 0.3 V vs. Na/Na$^+$, 1.5 g cm^{-3}) paired with industrially pursued CAMs, still exhibit a considerably lower energy content than LFP/graphite, gravimetrically (3–26% less Wh kg^{-1}), but particularly per volume (17–49% less Wh L^{-1}). Improving the electrochemical performance of HC, a current research objective, can narrow or even close this gap. Applying HC-optimized (375 mAh g^{-1}, 0.2 V vs. Na/Na$^+$, 1.8 g cm^{-3}) cells based on all three CAM classes reach competitive specific energies [Wh kg^{-1}] compared to the LIB benchmark. The energy density [Wh L^{-1}] of most SIB cells remains lower, most pronounced for PBA-based cells. However, the best performing SIB cells O3-ZNMT and O3-NFM surpass LFP/graphite regarding specific energy (+4–8% Wh kg^{-1}) and reach equal energy densities. Hence, layered oxide-based SIBs have the greatest potential to compete with LIBs in EV applications, at least in terms of energy density.

Furthermore, the importance of tailoring the electrode coating thicknesses is emphasized to achieve energy-optimized cells because the cell's energy content does not increase continuously with greater electrode thickness.

The results of the LCA indicate that, at the current development stage (HC-basic scenario), SIBs show cradle-to-gate CFs comparable but slightly higher than the benchmark LFP/graphite. The CF of LFP/graphite varies significantly depending on the type of graphite applied. LFP cells using SGr exhibit a CF of 76.1 kg CO$_2$-eq. kWh^{-1}, which is 35% higher than those entailing NGr at 56.5 kg CO$_2$-eq. kWh^{-1}. Given the current market share ($\sim$75% SGr, $\sim$25% NGr) and the increasing use of blended anodes, this study adopts a 75:25 SGr:NGr composition as the benchmark, yielding a CF of 71.2 kg CO$_2$-eq. kWh^{-1}.

Generally, the CF deviations across the analyzed cell chemistries are small ($\leq$17%). Only the NVPF cell (97.3 kg CO$_2$-eq. kWh^{-1}) and the LFP cell with 100% NGr (56.5 kg CO$_2$-eq. kWh^{-1}) deviate significantly from the benchmark. O3-ZNMT/HC is the SIB cell with the smallest CF at 71.6 kg CO$_2$-eq. kWh^{-1}.

The majority of GHGs, 80–87% of the CF, are attributed to material extraction and synthesis, and the remainder result from cell production. Particularly, the impact of the active materials is standing out, often making up more than 50% of the emissions. All SIB active materials have been assessed based on industry-scale data, including processing materials. New LCI data are provided for Na layered oxides, NVPF, NFPP and HC. For the synthesis of HC and the SGr precursor, needle coke, an unprecedented modeling approach, quantifying the energy produced from emerging volatiles is performed. The authors argue that energy generation from volatiles is substantial and has been neglected in previous work. Efficient capturing and energy generation from volatiles should be considered in HC synthesis plants to minimize energy costs and GHG emissions.

Energy generation from volatiles enables self-sustaining HC synthesis via carbonization, leading to low process emissions. The CF of pitch-based HC is 3.2 kg CO$_2$-eq. kg^{-1}, nearly half that of NGr (5.7 kg CO$_2$-eq. kg^{-1}), while SGr (25.1 kg CO$_2$-eq. kg^{-1}) even shows roughly eight times the impact of HC. The high CF of SGr primarily stems from the additional energy-intensive graphitization. Consequently, the use of HC enables SIBs to achieve competitive CFs to LIBs, despite their significantly lower energy density. Applying biomass-derived HC could further reduce the environmental impact, especially if SIBs exhibit long lifetimes, thus also function as long-term carbon storage. This would include the storage of biogenic carbon, resulting in nearly burden-free HC (e.g. 0.3 kg CO$_2$-eq. kg$^{-1}_{coconut-HC}$). In LIBs, the substitution of SGr with NGr significantly reduces the CF. However, given its lower purity, limited availability and the environmental burdens of mining, NGr's market share is expected to decrease even further. Therefore, it becomes essential to advance and scale graphite recycling techniques, an area that has been largely neglected within the industry.[258]

The analyzed SIB-CAMs demonstrate no environmental advantage compared to LFP. In contrast, LFP (7.6 kg CO$_2$-eq. kg^{-1}) has a lower CF than most SIB-CAMs, the only exception is polyanionic NFPP (5.8 kg CO$_2$-eq. kg^{-1}). For the layered oxides (all $\sim$15 kg CO$_2$-eq. kg^{-1}), the synthesis energy and the NiSO$_4$ precursor are emission hotspots. The CF of NVPF (22.0 kg CO$_2$-eq. kg^{-1}) and the PBAs (Fe-PBA: 9.0 kg CO$_2$-eq. kg^{-1}) mainly arise from a single precursor, V$_2$O$_5$ and Na$_4$Fe(CN)$_6$, respectively.

Based on this study and recent work[222,259] it can be assumed that most LCA studies underestimate the CF of battery active materials, often applying lab-scale LCI data. The consideration of production losses and detailed processing reagent data leads to significantly increased emission values. However, comprehensive primary industrial data are still scarce, even for LIB materials and should be a focus of future studies.

Additionally, two scenario analyses for enhancing environmental performance have been carried out. One aspect analyzed was the increase in energy density by applying HC-optimized. Secondly, aqueous cathode processing was modeled, replacing SOTA NMP-based production. Aqueous processing results in small GHG reductions with a cradle-to-gate CF decrease of 3–5%. The increase in energy density was found to be a more significant factor, reducing the CF of the SIB cells by 7–11%. Consequently, in the HC-optimized scenario, the majority of the assessed SIB cells exhibit smaller CFs than the LFP benchmark.

8122 | Energy Environ. Sci., 2025, **18**, 8104–8129

This journal is © The Royal Society of Chemistry 2025

Future studies could explore additional environmental impact categories, thereby examining other propagated environmental advantages of SIBs, such as the abundance and global distribution of Na compared to Li. Additionally, more comprehensive industrial synthesis data, specifically for SIB materials, is needed to enhance the accuracy of LCAs. Furthermore, future work should consider the use phase, including cycle life and cycling stability of SIB cells, as well as end-of-life treatment options, to provide a holistic environmental and technological assessment. For this purpose, real-life data from SIB cells implemented in applications should be incorporated, as such data are currently lacking. Moreover, future work should investigate the recycling of SIBs and explore strategies to overcome the limited economic incentive of SIB recycling, which stems from their comparatively low metal value.[260]

It can be concluded that SOTA SIBs show notably lower energy densities compared to LFP cells but already exhibit competitive CFs. Particularly, the AAMs play a critical role in the comparison of SIBs with the LFP benchmark. On the one hand, HC is the main bottleneck towards competitive energy densities, due to its inferior electrochemical performance relative to graphite applied in LIBs. On the other hand, the CF of HC is nearly a magnitude lower than that of SGr, enabling several SIB cell chemistries to exhibit comparable cradle-to-gate emissions to the LIB cell. Thus, enhancing the electrochemical performance of HC emerges as a key factor in order for SIBs to match the energy density of LFP cells, while further reducing the CF. Additionally, the most effective strategies to reduce GHG emissions involve energy-efficient CAM synthesis and minimization of high-impact precursors, such as $NiSO_4$, V_2O_5 and $Na_4Fe(CN)_6$.

Author contributions

Conceptualization PV, BG, SL; methodology PV, BG, SL; cell model PV, JDP; production model FD, PV, BG; synthesis modeling PV; LCA model BG, PV; supervision SL, visualization PV; writing – original draft PV (all parts), BG & MM (LCA-review); writing – review & editing PV, BG, RS, FD, SL; funding acquisition RS, SL; project administration SL; resources SL; validation PV.

Conflicts of interest

There are no conflicts to declare.

Data availability

The data supporting this article have been included as part of the ESI.† The production model applied in this work is mainly based on the model of Degen *et al.*, which can be found under "source data Fig. 3" at **https://doi.org/10.1038/s41560-023-01355-z**.

Acknowledgements

Notes and references

1 K. Riahi, D. P. van Vuuren, E. Kriegler, J. Edmonds, B. C. O'Neill, S. Fujimori, N. Bauer, K. Calvin, R. Dellink, O. Fricko, W. Lutz, A. Popp, J. C. Cuaresma, S. KC, M. Leimbach, L. Jiang, T. Kram, S. Rao, J. Emmerling, K. Ebi, T. Hasegawa, P. Havlik, F. Humpenöder, L. A. Da Silva, S. Smith, E. Stehfest, V. Bosetti, J. Eom, D. Gernaat, T. Masui, J. Rogelj, J. Strefler, L. Drouet, V. Krey, G. Luderer, M. Harmsen, K. Takahashi, L. Baumstark, J. C. Doelman, M. Kainuma, Z. Klimont, G. Marangoni, H. Lotze-Campen, M. Obersteiner, A. Tabeau and M. Tavoni, *Global Environ. Change*, 2017, **42**, 153–168.

2 F. Degen, M. Winter, D. Bendig and J. Tübke, *Nat. Energy*, 2023, **8**, 1–12.

3 F. Maisel, C. Neef, F. Marscheider-Weidemann and N. F. Nissen, *Resour., Conserv. Recycl.*, 2023, **192**, 106920.

4 L. Usai, J. J. Lamb, E. Hertwich, O. S. Burheim and A. H. Strømman, *Environ. Res.: Infrastruct. Sustainability*, 2022, **2**, 11002.

5 BloombergNEF, Lithium-Ion Battery Pack Prices Hit Record Low of $$139/kWh | BloombergNEF, **https://about.bnef. com/blog/lithium-ion-battery-pack-prices-hit-record-low-of-139-kwh/**.

6 M. S. Ziegler, J. Song and J. E. Trancik, *Energy Environ. Sci.*, 2021, **14**, 6074–6098.

7 G. Zubi, R. Dufo-López, M. Carvalho and G. Pasaoglu, *Renewable Sustainable Energy Rev.*, 2018, **89**, 292–308.

8 A. Wang and N. Yiu, Battery Component Price Report: March 2025, Intercalation, 2025.

9 C. M. Costa, J. C. Barbosa, R. Gonçalves, H. Castro, F. J. Del Campo and S. Lanceros-Méndez, *Energy Storage Mater.*, 2021, **37**, 433–465.

10 A. Masias, J. Marcicki and W. A. Paxton, *ACS Energy Lett.*, 2021, **6**, 621–630.

11 C. Vaalma, D. Buchholz, M. Weil and S. Passerini, *Nat. Rev. Mater.*, 2018, **3**, 1–11.

12 R. Usiskin, Y. Lu, J. Popovic, M. Law, P. Balaya, Y.-S. Hu and J. Maier, *Nat. Rev. Mater.*, 2021, **6**, 1020–1035.

13 J. Peters, A. Peña Cruz and M. Weil, *Batteries*, 2019, **5**, 10.

14 I. Hasa, J. Barker, G. Elia and S. Passerini, *Encyclopedia of Electrochemical Power Sources*, **vol. 2**.

15 Volta Foundation, The Battery Report 2024, 2025.

16 F. Duffner, N. Kronemeyer, J. Tübke, J. Leker, M. Winter and R. Schmuch, *Nat. Energy*, 2021, **6**, 123–134.

17 J.-Y. Hwang, S.-T. Myung and Y.-K. Sun, *Chem. Soc. Rev.*, 2017, **46**, 3529–3614.

This journal is © The Royal Society of Chemistry 2025

Energy Environ. Sci., 2025, **18**, 8104–8129 | **8123**

18 K. Nobuhara, H. Nakayama, M. Nose, S. Nakanishi and H. Iba, *J. Power Sources*, 2013, **243**, 585–587.

19 Y. Liu, B. V. Merinov and W. A. Goddard, *Proc. Natl. Acad. Sci. U. S. A.*, 2016, **113**, 3735–3739.

20 H. Moriwake, A. Kuwabara, C. A. J. Fisher and Y. Ikuhara, *RSC Adv.*, 2017, **7**, 36550–36554.

21 O. Lenchuk, P. Adelhelm and D. Mollenhauer, *Phys. Chem. Chem. Phys.*, 2019, **21**, 19378–19390.

22 Z. Wang, S. M. Selbach and T. Grande, *RSC Adv.*, 2014, **4**, 3973–3983.

23 L.-F. Zhao, Z. Hu, W.-H. Lai, Y. Tao, J. Peng, Z.-C. Miao, Y.-X. Wang, S.-L. Chou, H.-K. Liu and S.-X. Dou, *Adv. Energy Mater.*, 2021, **11**, 2002704.

24 H. Hou, X. Qiu, W. Wei, Y. Zhang and X. Ji, *Adv. Energy Mater.*, 2017, **7**, 1602898.

25 M. Thompson, Q. Xia, Z. Hu and X. S. Zhao, *Mater. Adv.*, 2021, **2**, 5881–5905.

26 F. Xie, Z. Xu, Z. Guo and M.-M. Titirici, *Prog. Energy*, 2020, **2**, 42002.

27 P. Adelhelm, P. Hartmann, C. L. Bender, M. Busche, C. Eufinger and J. Janek, *Beilstein J. Nanotechnol.*, 2015, **6**, 1016–1055.

28 J. Darga, J. Lamb and A. Manthiram, *Energy Technol.*, 2020, **8**, 2000723.

29 A. Rudola, A. J. R. Rennie, R. Heap, S. S. Meysami, A. Lowbridge, F. Mazzali, R. Sayers, C. J. Wright and J. Barker, *J. Mater. Chem. A*, 2021, **9**, 8279–8302.

30 J. F. Peters, M. Baumann, J. R. Binder and M. Weil, *Sustainable Energy Fuels*, 2021, **5**, 6414–6429.

31 H. Zhang, Y. Gao, X. Liu, L. Zhou, J. Li, Y. Xiao, J. Peng, J. Wang and S.-L. Chou, *Adv. Energy Mater.*, 2023, **13**, 2300149.

32 Y. Wang, R. Ou, J. Yang, Y. Xin, P. Singh, F. Wu, Y. Qian and H. Gao, *J. Energy Chem.*, 2024, **95**, 407–427.

33 M. He, A. E. Mejdoubi, D. Chartouni, M. Morcrette, P. Troendle and R. Castiglioni, *J. Power Sources*, 2023, **588**, 233741.

34 M. He, R. Davis, D. Chartouni, M. Johnson, M. Abplanalp, P. Troendle and R.-P. Suetterlin, *J. Power Sources*, 2022, **548**, 232036.

35 H. Yang, D. Wang, Y. Liu, Y. Liu, B. Zhong, Y. Song, Q. Kong, Z. Wu and X. Guo, *Energy Environ. Sci.*, 2024, **17**, 1756–1780.

36 C. Yang, S. Xin, L. Mai and Y. You, *Adv. Energy Mater.*, 2021, **11**, 2000974.

37 A. Yao, S. M. Benson and W. C. Chueh, *Nat. Energy*, 2025, **10**, 404–416.

38 I. Hasa, S. Mariyappan, D. Saurel, P. Adelhelm, A. Y. Koposov, C. Masquelier, L. Croguennec and M. Casas-Cabanas, *J. Power Sources*, 2021, **482**, 228872.

39 E. A. Olivetti, G. Ceder, G. G. Gaustad and X. Fu, *Joule*, 2017, **1**, 229–243.

40 M. A. Rajaeifar, P. Ghadimi, M. Raugei, Y. Wu and O. Heidrich, *Resour., Conserv. Recycl.*, 2022, **180**, 106144.

41 W.-H. Chen and I.-Y. L. Hsieh, *J. Cleaner Prod.*, 2023, **425**, 139045.

42 *Regulation (EU) 2023/1542 of the European Parliament and of the Council of 12 July 2023 concerning batteries and waste batteries, amending Directive* 2008/98/EC *and Regulation (EU)* 2019/1020 *and repealing Directive* 2006/66/EC, 2023.

43 IEA, Specifications for the Comprehensive Utilisation of Waste EV Batteries 2024 – Policies – IEA, **https://www.iea.org/policies/24987-specifications-for-the-comprehensive-utilisation-of-waste-ev-batteries-2024**.

44 S. Link, C. Neef and T. Wicke, *Batteries*, 2023, **9**, 261.

45 M. L. Terranova, S. Orlanducci, E. Tamburri, V. Guglielmotti and M. Rossi, *J. Power Sources*, 2014, **246**, 167–177.

46 Q. Liu, Y. Hu, X. Yu, Y. Qin, T. Meng and X. Hu, *Nano Res. Energy*, 2022, **1**, e9120037.

47 Z. Yang, Y. Yang, Z. Li, J. Wang, Y. Luo, J. Xie and H. Zhao, *Energy Mater. Adv.*, 2024, **4**, 0098.

48 J. Shi, Y. Li, K. Zhang, C. Wu and Y. Bai, *Mater. Sci. Eng., R*, 2025, **164**, 100954.

49 Z. Han, J. F. Wild, J. J. Chen and Y. Yang, *Energy Mater. Adv.*, 2024, **5**, 0111.

50 M. Greenwood, M. Wentker and J. Leker, *J. Power Sources Adv.*, 2021, **9**, 100055.

51 F. Xie, Z. Xu, Z. Guo, Y. Li, Y. Lu, M.-M. Titirici and Y.-S. Hu, in *Sodium-ion batteries. Materials, characterization, and technology*, ed. M.-M. Titirici, P. Adelhelm and Y. S. Hu, Wiley-VCH, Weinheim, 2023, vol. 23, pp. 27–59.

52 X. Dou, I. Hasa, D. Saurel, C. Vaalma, L. Wu, D. Buchholz, D. Bresser, S. Komaba and S. Passerini, *Mater. Today*, 2019, **23**, 87–104.

53 B. Xiao, T. Rojo and X. Li, *ChemSusChem*, 2019, **12**, 133–144.

54 M. Dahbi, N. Yabuuchi, K. Kubota, K. Tokiwa and S. Komaba, *Phys. Chem. Chem. Phys.*, 2014, **16**, 15007–15028.

55 B. Cao, H. Liu, B. Xu, Y. Lei, X. Chen and H. Song, *J. Mater. Chem. A*, 2016, **4**, 6472–6478.

56 X. Yao, Y. Ke, W. Ren, X. Wang, F. Xiong, W. Yang, M. Qin, Q. Li and L. Mai, *Adv. Energy Mater.*, 2019, **9**, 1803260.

57 S.-M. Zheng, Y.-R. Tian, Y.-X. Liu, S. Wang, C.-Q. Hu, B. Wang and K.-M. Wang, *Rare Met.*, 2021, **40**, 272–289.

58 K. Song, C. Liu, L. Mi, S. Chou, W. Chen and C. Shen, *Small*, 2021, **17**, e1903194.

59 E. Olsson and Q. Cai, in *Sodium-ion batteries. Materials, characterization, and technology*, ed. M.-M. Titirici, P. Adelhelm and Y. S. Hu, Wiley-VCH, Weinheim, 2023, pp. 259–300.

60 N. Tapia-Ruiz, A. R. Armstrong, H. Alptekin, M. A. Amores, H. Au, J. Barker, R. Boston, W. R. Brant, J. M. Brittain, Y. Chen, M. Chhowalla, Y.-S. Choi, S. I. R. Costa, M. Crespo Ribadeneyra, S. A. Cussen, E. J. Cussen, W. I. F. David, A. V. Desai, S. A. M. Dickson, E. I. Eweka, J. D. Forero-Saboya, C. P. Grey, J. M. Griffin, P. Gross, X. Hua, J. T. S. Irvine, P. Johansson, M. O. Jones, M. Karlsmo, E. Kendrick, E. Kim, O. V. Kolosov, Z. Li, S. F. L. Mertens, R. Mogensen, L. Monconduit, R. E. Morris, A. J. Naylor, S. Nikman, C. A. O'Keefe, D. M. C. Ould, R. G. Palgrave, P. Poizot, A. Ponrouch, S. Renault, E. M. Reynolds, A. Rudola, R. Sayers, D. O. Scanlon, S. Sen, V. R. Seymour, B. Silván, M. T. Sougrati, L. Stievano, G. S. Stone, C. I. Thomas, M.-M. Titirici, J. Tong, T. J. Wood, D. S. Wright and R. Younesi, *J. Phys.: Energy*, 2021, **3**, 31503.

8124 | *Energy Environ. Sci.*, 2025, **18**, 8104–8129

This journal is © The Royal Society of Chemistry 2025

61 A. Holland and S. Siddiqi, *Sodium-ion Batteries 2023–2033: Technology, Players, Markets, and Forecasts*, IDTechEx, 2023.

62 L. Mu, S. Xu, Y. Li, Y.-S. Hu, H. Li, L. Chen and X. Huang, *Adv. Mater.*, 2015, **27**, 6928–6933.

63 W. Zhang, Y. Zhang, J. Zhou, X. Li, W. Zhou, D. Zhang, J. Mao and K. Dai, *J. Electrochem. Soc.*, 2023, **170**, 70518.

64 Liyang Hina Battery Tech Co Ltd, CN114843499 (A), 2022.

65 J. Abou-Rjeily, Na-ion battery development @ TIAMAT, 5th International Sodium Battery Symposium-Berlin, 2024.

66 S. Mariyappan, T. Marchandier, F. Rabuel, A. Iadecola, G. Rousse, A. V. Morozov, A. M. Abakumov and J.-M. Tarascon, *Chem. Mater.*, 2020, **32**, 1657–1666.

67 J.-M. Tarascon, *Joule*, 2020, **4**, 1616–1620.

68 F. Dorau, A. Sommer, J. Koloch, R. Roess-Ohlenroth, M. Schreiber, M. Neuner, K. Abo Gamra, Y. Lin, J. Schöberl, P. Bilfinger, S. Grabmann, B. Stumper, L. Katzenmeier, M. Lienkamp and R. Daub, *J. Electrochem. Soc.*, 2024, **171**, 90521.

69 H. Laufen, S. Klick, H. Ditler, K. L. Quade, A. Mikitisin, A. Blömeke, M. Schütte, D. Wasylowski, M. Sonnet, L. Henrich, A. Schwedt, G. Stahl, F. Ringbeck, J. Mayer and D. U. Sauer, *Cell Rep. Phys. Sci.*, 2024, **5**, 101945.

70 L. Streck, T. Roth, H. Bosch, C. Kirst, M. Rehm, P. Keil and A. Jossen, *J. Electrochem. Soc.*, 2024, **171**, 80531.

71 V. Marangon, K. Bischof, A. A. Regalado, M. Keppeler, M. Pogosova, M. Wan, J. Choi, S. Fleischmann, T. Diemant, M. Wohlfahrt-Mehrens, M. Hölzle, T. Waldmann and D. Bresser, *J. Power Sources*, 2025, **634**, 236496.

72 K. Bischof, V. Marangon, M. Kasper, A. Aracil Regalado, M. Wohlfahrt-Mehrens, M. Hölzle, D. Bresser and T. Waldmann, *J. Power Sources Adv.*, 2024, **27**, 100148.

73 T. Hettesheimer, C. Neef, I. Rosellón Inclán, S. Link, T. Schmaltz, F. Schuckert, A. Stephan, M. Stephan, A. Thielmann, L. Weymann and T. Wicke, Lithium-Ion Battery Roadmap – Industrialization Perspectives toward 2030, Fraunhofer ISI, 2023.

74 Ningbo Ronbay Lithium Battery Material Co Ltd, CN115966686 (A), 2023.

75 Ningbo Ronbay Lithium Battery Material Co Ltd, CN116525809 (A), 2023.

76 Ningbo Ronbay Lithium Battery Material Co Ltd, CN116525813 (A), 2023.

77 Ningbo Ronbay Lithium Battery Material Co Ltd, CN116544417 (A), 2023.

78 Ningbo Ronbay Lithium Battery Material Co Ltd, CN116199275 (A), 2023.

79 Ningbo Ronbay Lithium Battery Material Co Ltd, CN117199342 (A), 2023.

80 BTR New Material Group, Layered Transition Metal Oxides for SIB Cathode Material, https://www.btrchina.com/en/CathodeProducts/info.aspx?itemid=937.

81 CATL, Naxtra Battery Breakthrough & Dual-Power Architecture: CATL Pioneers the Multi-Power Era, https://www.catl.com/en/news/6401.html.

82 Contemporary Ampex Tech Co Limited, US2022123299 (A1), 2021.

83 Contemporary Amperex Technology Co Ltd, US2021167375 (A1), 2021.

84 Contemporary Amperex Technology Co Ltd, US2024194867 (A1), 2024.

85 Ningde Contemporary Amperex Tech Co Ltd, CN116314728 (A), 2023.

86 Shanghai Metals Market, Sodium battery production and sales in October increased MoM. Market activity surged significantly., https://news.metal.com/newscontent/103085355/sodium-battery-production-and-sales-in-october-increased-mom-market-activity-surged-significantly-smm-sodium-battery-analysis.

87 Jiana Energy, JNFP-1, https://www.janaenergy.com/pd.jsp?id=13.

88 Zhejiang NaTRIUM Energy, Series NFPP Model NPA-11T01, https://www.natrium-energy.cn/en/view/223.html.

89 Shanghai Metals Market, Sodium-ion Batteries: BYD and Nachuang Win the Bid for NFPP Energy Storage R&D Project, https://news.metal.com/newscontent/102857456.

90 Shenzhen Jiana Energy Tech Co Ltd, CN117585659 (A), 2023.

91 Ningbo Ronbay Lithium Battery Material Co Ltd, CN117577831 (A), 2023.

92 H. Kim, I. Park, D.-H. Seo, S. Lee, S.-W. Kim, W. J. Kwon, Y.-U. Park, C. S. Kim, S. Jeon and K. Kang, *J. Am. Chem. Soc.*, 2012, **134**, 10369–10372.

93 Shenzhen Jiana Energy Tech Co Ltd, CN119503750 (A), 2024.

94 L. Li, J. Meng, X. Kong, P. Lin, Q. Rong, X. Jiao, Z. Song, Y. Liu and S. Ding, *J. Mater. Chem. A*, 2025, **13**, 16274.

95 Zhejiang NaTRIUM Energy, Sodium ferric sulfate Model NPA-01T1, https://www.natrium-energy.cn/en/view/239.html.

96 Jiana Energy, JNFS-1, https://www.janaenergy.com/pd.jsp?id=15.

97 Zhenjiang Lina Energy Tech Co Ltd and Jiangsu Zhongna Energy Tech Co Ltd, CN118579846 (A), 2024.

98 A. Plewa, A. Kulka, E. Hanc, W. Zając, J. Sun, L. Lu and J. Molenda, *J. Mater. Chem. A*, 2020, **8**, 2728–2740.

99 S. Li, X. Song, X. Kuai, W. Zhu, K. Tian, X. Li, M. Chen, S. Chou, J. Zhao and L. Gao, *J. Mater. Chem. A*, 2019, **7**, 14656–14669.

100 Jiana Energy, Jiana Energy launches the world's first 10 000-ton production line for polyanionic sodium-ion battery cathode materials: ushering in a new era for the sodium-ion battery industry [ENG translation], https://www.janaenergy.com/nd.jsp?id=39.

101 Shenzhen Jiana Energy Tech Co Ltd, CN118221093 (A), 2024.

102 Ningbo Ronbay New Energy Tech Co Ltd [CN], WO2025002138 (A1), 2024.

103 Zhejiang Nachuang New Energy Co Ltd, CN117361482 (A), 2023.

104 Shanghai Metals Market, NFPP 10 000 mt Production Lines Successively Put into Operation: Innovation in Sodium-Ion Battery Cathode Materials and Reshaping of Market Landscape, https://www.metal.com/en/newscontent/103322888.

105 Zoolnasm, Zhongna Energy's Guangde Xunna sodium-ion battery manufacturing base project started [ENG translation],

This journal is © The Royal Society of Chemistry 2025

Energy Environ. Sci., 2025, **18**, 8104–8129 | **8125**

https://www.zoolnasm.com/?m=home&c=View&a=index&aid=634.

106 Northvolt, Northvolt develops state-of-the-art sodium-ion battery validated at 160 Wh kg^{-1}, https://northvolt.com/articles/northvolt-sodium-ion/.

107 Altris, Altris presents world-leading Prussian White cathode material, https://www.altris.se/news/altris-presents-world-leading-prussian-white-cathode-material.

108 H. Liu, M. Baumann, X. Dou, J. Klemens, L. Schneider, A.-K. Wurba, M. Häringer, P. Scharfer, H. Ehrenberg, W. Schabel, J. Fleischer, N. von der Aßen and M. Weil, J. Energy Storage, 2022, 56, 105964.

109 L. Xiao, H. Lu, Y. Fang, M. L. Sushko, Y. Cao, X. Ai, H. Yang and J. Liu, Adv. Energy Mater., 2018, 8, 1703238.

110 M. Zhang, Y. Li, F. Wu, Y. Bai and C. Wu, Nano Energy, 2021, 82, 105738.

111 E. Irisarri, N. Amini, S. Tennison, C. M. Ghimbeu, J. Gorka, C. Vix-Guterl, A. Ponrouch and M. R. Palacin, J. Electrochem. Soc., 2018, 165, A4058–A4066.

112 C. M. Del Saavedra Rios, V. Simone, L. Simonin, S. Martinet and C. Dupont, Biomass Bioenergy, 2018, 117, 32–37.

113 C. Del Mar Saavedra Rios, L. Simonin, C. M. Ghimbeu, C. Vaulot, D. Da Silva Perez and C. Dupont, Fuel Process. Technol., 2022, 231, 107223.

114 W. Wang, B. Wang, Y. Li, N. Wang, Y. Xu, C. Wang, Y. Sun and H. Hu, Chem. – Asian J., 2024, 19, e202301146.

115 T. Liu and X. Li, Mater. Technol., 2019, 34, 232–245.

116 X. Zhang, S. Han, C. Fan, L. Li and W. Zhang, J. Solid State Electrochem., 2015, 19, 715–721.

117 J. Xiang, W. Lv, C. Mu, J. Zhao and B. Wang, J. Alloys Compd., 2017, 701, 870–874.

118 Z. Xu, J. Chen, M. Wu, C. Chen, Y. Song and Y. Wang, Electron. Mater. Lett., 2019, 15, 428–436.

119 A. Gomez-Martin, J. Martinez-Fernandez, M. Ruttert, M. Winter, T. Placke and J. Ramirez-Rico, Chem. Mater., 2019, 31, 7288–7299.

120 Y. Li, Y. Lu, Q. Meng, A. C. S. Jensen, Q. Zhang, Q. Zhang, Y. Tong, Y. Qi, L. Gu, M.-M. Titirici and Y.-S. Hu, Adv. Energy Mater., 2019, 9, 1902852.

121 DIN EN ISO 14040:2021-02, Umweltmanagement_- Ökobilanz_- Grundsätze und Rahmenbedingungen (ISO_14040:2006_+ Amd_1:2020), DIN Media GmbH, Berlin.

122 J. Peters, D. Buchholz, S. Passerini and M. Weil, Energy Environ. Sci., 2016, 9, 1744–1751.

123 S. F. Schneider, C. Bauer, P. Novák and E. J. Berg, Sustainable Energy Fuels, 2019, 3, 3061–3070.

124 Faradion Ltd, US2015194672 (A1), 2013.

125 Faradion Ltd, US2016329564 (A1), 2015.

126 Faradion Ltd, US2021155501 (A1), 2019.

127 D. D. Yuan, Y. X. Wang, Y. L. Cao, X. P. Ai and H. X. Yang, ACS Appl. Mater. Interfaces, 2015, 7, 8585–8591.

128 H. Wang, F. Ding, Y. Wang, Z. Han, R. Dang, H. Yu, Y. Yang, Z. Chen, Y. Li, F. Xie, S. Zhang, H. Zhang, D. Song, X. Rong, L. Zhang, J. Xu, W. Yin, Y. Lu, R. Xiao, D. Su, L. Chen and Y.-S. Hu, ACS Energy Lett., 2023, 8, 1434–1444.

129 Q. Liu, D. Wang, X. Yang, N. Chen, C. Wang, X. Bie, Y. Wei, G. Chen and F. Du, J. Mater. Chem. A, 2015, 3, 21478–21485.

130 H. Yi, L. Lin, M. Ling, Z. Lv, R. Li, Q. Fu, H. Zhang, Q. Zheng and X. Li, ACS Energy Lett., 2019, 4, 1565–1571.

131 T. Broux, F. Fauth, N. Hall, Y. Chatillon, M. Bianchini, T. Bamine, J.-B. Leriche, E. Suard, D. Carlier, Y. Reynier, L. Simonin, C. Masquelier and L. Croguennec, Small Methods, 2019, 3, 1800215.

132 Y.-Q. Zheng, M.-Y. Sun, F.-D. Yu, L. Deng, Y. Xia, Y.-S. Jiang, L.-F. Que, L. Zhao and Z.-B. Wang, Nano Energy, 2022, 102, 107693.

133 Altris Ab, WO2018056890 (A1), 2017.

134 Y. P. Wang, B. P. Hou, X. R. Cao, S. Q. Wu and Z. Z. Zhu, J. Electrochem. Soc., 2022, 169, 10525.

135 L. Wang, J. Song, R. Qiao, L. A. Wray, M. A. Hossain, Y.-D. Chuang, W. Yang, Y. Lu, D. Evans, J.-J. Lee, S. Vail, X. Zhao, M. Nishijima, S. Kakimoto and J. B. Goodenough, J. Am. Chem. Soc., 2015, 137, 2548–2554.

136 K. Wu, X. Dou, X. Zhang and C. OuYang, Engineering, 2023, 21, 36–38.

137 Contemporary Amperex Technology Co., Ltd., Sodium-ion battery press conference, https://www.catl.com/technology brand/6251.html.

138 Contemporary Amperex Technology Co., Ltd., CATL Unveils Its Latest Breakthrough Technology by Releasing Its First Generation of Sodium-ion Batteries, https://www.catl.com/en/news/665.html.

139 Contemporary Amperex Technology Co Ltd, US2023227321 (A1), 2023.

140 P. Xiao, J. Song, L. Wang, J. B. Goodenough and G. Henkelman, Chem. Mater., 2015, 27, 3763–3768.

141 J. Song, L. Wang, Y. Lu, J. Liu, B. Guo, P. Xiao, J.-J. Lee, X.-Q. Yang, G. Henkelman and J. B. Goodenough, J. Am. Chem. Soc., 2015, 137, 2658–2664.

142 F. Ding, C. Zhao, D. Xiao, X. Rong, H. Wang, Y. Li, Y. Yang, Y. Lu and Y.-S. Hu, J. Am. Chem. Soc., 2022, 144, 8286–8295.

143 M. Chen, W. Hua, J. Xiao, D. Cortie, W. Chen, E. Wang, Z. Hu, Q. Gu, X. Wang, S. Indris, S.-L. Chou and S.-X. Dou, Nat. Commun., 2019, 10, 1480.

144 P. Barpanda, G. Oyama, S. Nishimura, S.-C. Chung and A. Yamada, Nat. Commun., 2014, 5, 4358.

145 X. Zhao, L. Zhang, X. Wang, J. Li, L. Zhang, D. Liu, R. Yang, X. Jin, M. Sui and P. Yan, J. Mater. Chem. A, 2024, 12, 11681–11690.

146 Beijing Hina Battery Tech Co Ltd and Inst of Physics the Chinese Academy of Sciences, US2021202942 (A1), 2018.

147 JFE Chemical Corporation, Battery materials, https://www.jfe-chem.com/en/product/battery/.

148 R. Haga, Development of Hard Carbon Anode Material from Coal-Tar Pitch, 2022.

149 Y. Tianjin Carbon, Hard carbon negative electrode materials for sodium/lithium batteries, https://www.tianjinyu feng.com/cpzs/html/9.html.

150 Tianjin Yufeng Carbon Co Ltd, CN115188952 (A), 2022.

151 S. Kuze, J. Kageura, S. Matsumoto, T. Nakayam, M. Makidera, M. Saka, T. Yamaguchi, T. Yamamoto and K. Nakane, R&D Report, SUMITOMO KAGAKU, 2013.

8126 | Energy Environ. Sci., 2025, 18, 8104–8129

This journal is © The Royal Society of Chemistry 2025

152 Wuhan Bixidi Cell Mat Co Ltd, CN112645306 (A), 2021.

153 AT Electrode, Electrode material BELLFINE®, https://at-electrode.com/bellfine/.

154 H. Moon, M. Zarrabeitia, E. Frank, O. Böse, M. Enterría, D. Saurel, I. Hasa and S. Passerini, *Batteries Supercaps*, 2021, **4**, 960–977.

155 Shengquan Group, Hard Carbon Anode Materials, https://www.shengquan.com/product/118.html.

156 Kuraray, KURANODE™ BIOHARDCARBON, https://www.calgoncarbon.com/app/uploads/KN-brochure-EN-002.pdf.

157 Kuraray, New Factory Completed for BIOCARBOTRON, Plant-Based Hard Carbon Anode Material for Lithium-Ion Batteries, https://www.kuraray.com/news/2014/140408.

158 HaycarbPLC, HARD CARBON (HCH102), https://www.haycarb.com/wp-content/uploads/2023/07/Hard-Carbon-Brochure.pdf.

159 Stora Enso, Lignode®: The powerful potential of trees, https://www.storaenso.com/en/products/lignin/lignode.

160 UP Catalyst, Hard carbon – UP Catalyst, https://upcatalyst.com/hard-carbon/.

161 BTR New Material Group, Hard carbon-BSHC series, https://www.btrchina.com/en/NegativeProducts/info.aspx?itemid=1063.

162 Shenzhen Fengghua Science and Tech Co Ltd and Fujian Fengghua New Energy Mat Co Ltd, CN114477130 (A), 2021.

163 Shenzhen Xiangfenghua Tech Co Ltd, Sichuan Xfh New Energy Mat Co Ltd and Fujian Xfh Battery Mat Co Ltd, CN116534835 (A), 2023.

164 Shenzhen Xiangfenghua Tech Co Ltd, Fujian Xfh Battery Mat Co Ltd and Shanghai Xiangfenghua Tech Development Co Ltd, CN116169238 (A), 2022.

165 Shenzhen Xiangfenghua Tech Co Ltd, Sichuan Xfh New Energy Mat Co Ltd and Fujian Xfh New Energy Mat Co Ltd, CN114709393 (A), 2022.

166 Liyang Hina Battery Tech Co Ltd and Beijing Hina Battery Tech Co Ltd, CN114956037 (A), 2022.

167 Shanshan Technology, New materials, https://shanshantech.com/new-type-materials.

168 Shanshan Technology, Shanshan Times 2022.11.30.

169 Aekyung Chemical, Anode – PAC-2, https://www.aekyungchemical.co.kr/eng/business/bio-energy.html.

170 Best Graphite, SIB Hard carbon NHC-330, https://www.cdbsg.com/index/news/detail.html?id=125&cid=15&pid=3.

171 Best Graphite, SIB Hard carbon YHC-2, https://www.cdbsg.com/index/news/detail.html?id=127&cid=15&pid=3.

172 Shinzoom Technology, Hard carbon, https://www.shinzoom.com/product/39.html.

173 Shanghai Putailai, Anode Materials and Graphitization-Shanghai PTL New Energy Technology, https://www.putailai.com/en/business-products/anode-materials-and-graphitization.

174 Y. Li, Y.-S. Hu, X. Qi, X. Rong, H. Li, X. Huang and L. Chen, *Energy Storage Mater.*, 2016, **5**, 191–197.

175 Liyang Hina Battery Tech Co Ltd and Beijing Hina Battery Tech Co Ltd, CN111293309 (A), 2020.

176 Inst Physics Cas and Beijing Hina Battery Tech Co Ltd, WO2019062495 (A1), 2018.

177 S. Wickerts, R. Arvidsson, A. Nordelöf, M. Svanström and P. Johansson, *J. Ind. Ecol.*, 2024, **28**, 116–129.

178 M. Baumann, M. Häringer, M. Schmidt, L. Schneider, J. F. Peters, W. Bauer, J. R. Binder and M. Weil, *Adv. Energy Mater.*, 2022, **12**, 2202636.

179 J. F. Peters, M. Abdelbaky, M. Baumann and M. Weil, *Mater. Tech.*, 2019, **107**, 503.

180 *Organic Waste for the Production of Hard Carbon for Batteries - A Life Cycle Assessment Perspective. 9th International Symposium Circular Economy, MBT, MRF and Recycling*, ed. H. Liu, C. R. Tomasini, L. Lan, J. Li, X. Zhang, N. Aßen and M. Weil, Cuvillier Verlag, Göttingen, 1st edn, 2021.

181 H. Liu, M. Baumann, H. Moon, X. Zhang, X. Dou, M. Zarrabeitia, E. Crenna, R. Hischier, S. Passerini, N. von der Assen and M. Weil, *Chem. Eng. J.*, 2024, **495**, 153410.

182 Y. Chu, J. Zhang, Y. Zhang, Q. Li, Y. Jia, X. Dong, J. Xiao, Y. Tao and Q.-H. Yang, *Adv. Mater.*, 2023, **35**, e2212186.

183 A. Mehmood, G. Ali, B. Koyutürk, J. Pampel, K. Y. Chung and T.-P. Fellinger, *Energy Storage Mater.*, 2020, **28**, 101–111.

184 Y. Yang, C. Wu, X.-X. He, J. Zhao, Z. Yang, L. Li, X. Wu, L. Li and S.-L. Chou, *Adv. Funct. Mater.*, 2024, **34**, 2302277.

185 T. Krause, D. Nusko, L. Pitta Bauermann, M. Vetter, M. Schäfer and C. Holly, *Energies*, 2024, **17**, 1566.

186 C. Zhao, T. Wada, V. de Andrade, D. Gürsoy, H. Kato and Y. K. Chen-Wiegart, *Nano Energy*, 2018, **52**, 381–390.

187 T. Deich, M. Storch, K. Steiner and A. Bund, *J. Power Sources*, 2021, **506**, 230163.

188 T. Deich, S. L. Hahn, S. Both, K. P. Birke and A. Bund, *J. Energy Storage*, 2020, **28**, 101192.

189 R. Bernhard, M. Metzger and H. A. Gasteiger, *J. Electrochem. Soc.*, 2015, **162**, A1984–A1989.

190 C. Schulze and K. P. Birke, *J. Energy Storage*, 2022, **55**, 105736.

191 M. Winter, G. H. Wrodnigg, J. O. Besenhard, W. Biberacher and P. Novák, *J. Electrochem. Soc.*, 2000, **147**, 2427.

192 M. Hahn, H. Buqa, P. W. Ruch, D. Goers, M. E. Spahr, J. Ufheil, P. Novák and R. Kötz, *Electrochem. Solid-State Lett.*, 2008, **11**, A151.

193 H. Michael, F. Iacoviello, T. M. M. Heenan, A. Llewellyn, J. S. Weaving, R. Jervis, D. J. L. Brett and P. R. Shearing, *J. Electrochem. Soc.*, 2021, **168**, 10507.

194 F. B. Spingler, S. Kücher, R. Phillips, E. Moyassari and A. Jossen, *J. Electrochem. Soc.*, 2021, **168**, 40515.

195 D. Ren, L. Xie, L. Wang and X. He, *Int. J. Energy Res.*, 2021, **45**, 7732–7740.

196 W. H. Woodford, W. C. Carter and Y.-M. Chiang, *Energy Environ. Sci.*, 2012, **5**, 8014.

197 D. Clerici, F. Mocera and A. Somà, *J. Power Sources*, 2022, **542**, 231735.

198 H. Alptekin, H. Au, A. C. S. Jensen, E. Olsson, M. Goktas, T. F. Headen, P. Adelhelm, Q. Cai, A. J. Drew and M.-M. Titirici, *ACS Appl. Energy Mater.*, 2020, **3**, 9918–9927.

199 I. Escher, G. A. Ferrero, M. Goktas and P. Adelhelm, *Adv. Mater. Interfaces*, 2022, **9**, 2100596.

200 I. Escher, M. Hahn, G. A. Ferrero and P. Adelhelm, *Energy Technol.*, 2022, **10**, 2101120.

This journal is © The Royal Society of Chemistry 2025

Energy Environ. Sci., 2025, **18**, 8104–8129 | 8127

201 B. Rieger, S. Schlueter, S. V. Erhard and A. Jossen, *J. Electrochem. Soc.*, 2016, **163**, A1595–A1606.

202 B. Rieger, S. V. Erhard, K. Rumpf and A. Jossen, *J. Electrochem. Soc.*, 2016, **163**, A1566–A1575.

203 F. Degen and M. Schütte, *J. Cleaner Prod.*, 2022, **330**, 129798.

204 F. Degen and O. Krätzig, *IEEE Trans. Eng. Manage.*, 2024, **71**, 6753–6769.

205 K. Momma and F. Izumi, *J. Appl. Crystallogr.*, 2011, **44**, 1272–1276.

206 S. Ahmed, P. A. Nelson, K. G. Gallagher and D. W. Dees, *J. Power Sources*, 2016, **322**, 169–178.

207 L. Ibing, T. Gallasch, P. Schneider, P. Niehoff, A. Hintennach, M. Winter and F. M. Schappacher, *J. Power Sources*, 2019, **423**, 183–191.

208 L. Ibing, T. Gallasch, V. Göken, P. Niehoff, M. Winter and M. Börner, *ACS Appl. Energy Mater.*, 2022, **5**, 13155–13160.

209 D. L. Wood, J. D. Quass, J. Li, S. Ahmed, D. Ventola and C. Daniel, *Drying Technol.*, 2018, **36**, 234–244.

210 Q. Dai, J. C. Kellly, J. Dunn and P. T. Benavides, Update of Bill-of-Materials and Cathode Materials Production for Lithium-ion Batteries in the GREET® Model, 2018.

211 Q. Liu, Z. Hu, M. Chen, C. Zou, H. Jin, S. Wang, S.-L. Chou, Y. Liu and S.-X. Dou, *Adv. Funct. Mater.*, 2020, **30**, 1909530.

212 W.-J. Li, C. Han, W. Wang, F. Gebert, S.-L. Chou, H.-K. Liu, X. Zhang and S.-X. Dou, *Adv. Energy Mater.*, 2017, **7**, 1700274.

213 V. P. Mhaske, S. Jilkar and M. D. Yadav, *Energy Fuels*, 2023, **37**, 16221–16244.

214 J. Lamb and A. Manthiram, *Chem. Mater.*, 2020, **32**, 8431–8441.

215 J. Quan, S. Zhao, D. Song, T. Wang, W. He and G. Li, *Sci. Total Environ.*, 2022, **819**, 153105.

216 Commissariat Energie Atomique, Centre Nat Rech Scient and Univ de Picardie Jules Vernes, US2018297847 (A1), 2016.

217 L. Huang, C. Liu, L. Bao, Y. Chen, Y. Jiang and X. Fu, *ACS Appl. Energy Mater.*, 2023, **6**, 11541–11549.

218 P. Li, B. Li, Z. Liu and Y. Yu, *Therm. Sci.*, 2022, **26**, 1809–1823.

219 E. M. Elkanzi, *Chem. Prod. Process Model.*, 2007, **2**, 20.

220 R. T. Bui, J. Perron and M. Read, *Carbon*, 1993, **31**, 1139–1147.

221 R. Zarzycki, R. Kobyłecki and Z. Bis, *Entropy*, 2020, **22**, 181.

222 T. Carrère, U. Khalid, M. Baumann, M. Bouzidi and B. Allard, *J. Energy Storage*, 2024, **94**, 112356.

223 P. Engels, F. Cerdas, T. Dettmer, C. Frey, J. Hentschel, C. Herrmann, T. Mirfabrikikar and M. Schueler, *J. Cleaner Prod.*, 2022, **336**, 130474.

224 T. Mendiara, A. Navajas, A. Abad, T. Pröll, M. Munárriz, L. M. Gandía, F. García-Labiano and L. F. de Diego, *Sustainability*, 2024, **16**, 4013.

225 *Anyang General Chemical*, Coal Tar Pitch | CAS 8052-42-4, https://www.lookforchem.com/Products/Organic-Chemicals/coal-tar-pitch-cas-8052-42-4.html.

226 S. M. Lee, S. H. Lee and D.-H. Jung, *Sci. Rep.*, 2021, **11**, 1460.

227 M. S. Hosseini and P. Chartrand, *Fuels*, 2022, **3**, 698–729.

228 D. Kocaefe, Y. Xie, Y. Kocaefe, L. Wei, S. Zou and A. Wu, *JMSR*, 2013, **2**, p22.

229 E. Irisarri, N. Amini, S. Tennison, C. M. Ghimbeu, J. Gorka, C. Vix-Guterl, A. Ponrouch and M. R. Palacin, *J. Electrochem. Soc.*, 2018, **165**, A4058–A4066.

230 A. Bennett, D. Payne and R. Court, *51st AIAA Aerospace Sciences Meeting including the New Horizons Forum and Aerospace Exposition*, 2013.

231 D. Chen, K. Cen, X. Zhuang, Z. Gan, J. Zhou, Y. Zhang and H. Zhang, *Combust. Flame*, 2022, **242**, 112142.

232 S. D. Stefanidis, K. G. Kalogiannis, E. F. Iliopoulou, C. M. Michailof, P. A. Pilavachi and A. A. Lappas, *J. Anal. Appl. Pyrolysis*, 2014, **105**, 143–150.

233 Z. Zheng, Y. Wang, Y. Zhang, X. Li, Y. Zhang, Y.-S. He, H. Che, L. Li and Z.-F. Ma, *Nano Energy*, 2024, **128**, 109907.

234 J. Gao, H. Chen, Y. Mei, L. Ni, H. Wang, J. Huang, N. Hong, B. Song, Y. Tian, W. Deng, G. Zou, H. Hou and X. Ji, *Nano Energy*, 2023, **115**, 108747.

235 D. Andre, H. Hain, P. Lamp, F. Maglia and B. Stiaszny, *J. Mater. Chem. A*, 2017, **5**, 17174–17198.

236 Y. Son, H. Cha, C. Jo, A. S. Groombridge, T. Lee, A. Boies, J. Cho and M. de Volder, *Mater. Today Energy*, 2021, **21**, 100838.

237 Y. Kim, M. Kim, T. Lee, E. Kim, M. An, J. Park, J. Cho and Y. Son, *Electrochem. Commun.*, 2023, **147**, 107437.

238 K. Bhuwalka, H. Ramachandran, S. Narasimhan, A. Yao, J. Frohmann, L. Peiseler, W. Chueh, A. Boies, S. J. Davis and S. Benson, *Securing the supply of graphite for batteries*, 2025.

239 Rystad Energy, *Fake it till you make it: Synthetic graphite holds the key to meeting battery demand surge, despite ESG concerns*, https://www.rystadenergy.com/news/fake-it-till-you-make-it-synthetic-graphite-holds-the-key-to-meeting-battery-dema.

240 Benchmark Mineral Intelligence, Infographic: China controls three-quarters of graphite anode supply chain, https://source.benchmarkminerals.com/article/infographic-china-controls-three-quarters-of-graphite-anode-supply-chain.

241 J. B. Dunn, C. James, L. Gaines, K. Gallagher, Q. Dai and J. C. Kelly, *Material and Energy Flows in the Production of Cathode and Anode Materials for Lithium Ion Batteries*, 2015.

242 D. Surovtseva, E. Crossin, R. Pell and L. Stamford, *J. Ind. Ecol.*, 2022, **26**, 964–979.

243 R. Iyer and J. Kelly, Updated Production Inventory for Lithium-Ion Battery Anodes for the GREET® Model, and Review of Advanced Battery Chemistries ANL-22/74, 2022.

244 S. Chen, X. Fu, M. Chu, Z. Liu and J. Tang, *J. Cleaner Prod.*, 2015, **101**, 122–128.

245 U.S. Geological Survey, Mineral Commodity Summaries, 2024.

246 Y. Liu, H. Liu, R. Zhang, Y. Zhong, Z. Wu, X. Wang and Z. Zhang, *Ionics*, 2024, **30**, 39–59.

247 H.-J. Althaus, R. Hischier, M. Osses, A. Primas, S. Hellweg, N. Jungbluth and M. Chudacoff, *Life cycle inventories of chemicals*, 2007.

248 M. Lechner, A. Kollenda, K. Bendzuck, J. K. Burmeister, K. Mahin, J. Keilhofer, L. Kemmer, M. J. Blaschke, G. Friedl, R. Daub and A. Kwade, *Commun. Eng.*, 2024, **3**, 155.

8128 | *Energy Environ. Sci.*, 2025, **18**, 8104–8129

This journal is © The Royal Society of Chemistry 2025

249 X. Hu, A. K. J. An and S. S. Chopra, *ACS Sustainable Chem. Eng.*, 2022, **10**, 5708–5718.

250 A. Hunt and N. Dale, *OECD Environment Working Papers*, OECD, 2018, vol. 131.

251 Y. Lu, K. Peng and L. Zhang, *ACS ES&T Eng.*, 2022, **2**, 586–605.

252 L. Azhari, X. Zhou, B. Sousa, Z. Yang, G. Gao and Y. Wang, *ACS Appl. Mater. Interfaces*, 2020, **12**, 57963–57974.

253 W. B. Hawley, A. Parejiya, Y. Bai, H. M. Meyer, D. L. Wood and J. Li, *J. Power Sources*, 2020, **466**, 228315.

254 W. Bauer, F. A. Çetinel, M. Müller and U. Kaufmann, *Electrochim. Acta*, 2019, **317**, 112–119.

255 I. de Meatza, I. Urdampilleta, I. Boyano, I. Castrillo, I. Landa-Medrano, S. Sananes-Israel, A. Eguia-Barrio and V. Palomares, *J. Electrochem. Soc.*, 2023, **170**, 10527.

256 M. Kuenzel, D. Bresser, T. Diemant, D. V. Carvalho, G.-T. Kim, R. J. Behm and S. Passerini, *ChemSusChem*, 2018, **11**, 562–573.

257 M. Wood, J. Li, R. E. Ruther, Z. Du, E. C. Self, H. M. Meyer, C. Daniel, I. Belharouak and D. L. Wood, *Energy Storage Mater.*, 2020, **24**, 188–197.

258 M. Abdollahifar, S. Doose, H. Cavers and A. Kwade, *Adv. Mater. Technol.*, 2023, **8**, 2200368.

259 R. Istrate, A. Mas-Fons, A. Beylot, S. Northey, K. Vaidya, G. Sonnemann, R. Kleijn and B. Steubing, *Joule*, 2024, **8**, 2992–3016.

260 Y. Zhao, Y. Kang, J. Wozny, J. Lu, H. Du, C. Li, T. Li, F. Kang, N. Tavajohi and B. Li, *Nat. Rev. Mater.*, 2023, **8**, 623–634.

This journal is © The Royal Society of Chemistry 2025

Energy Environ. Sci., 2025, **18**, 8104–8129 | 8129